



HAL
open science

A Kalman Filter Time Series Analysis Method for InSAR

M. Dalaison, Romain Jolivet

► **To cite this version:**

M. Dalaison, Romain Jolivet. A Kalman Filter Time Series Analysis Method for InSAR. *Journal of Geophysical Research: Solid Earth*, 2020, 125 (7), pp.e2019JB019150. 10.1029/2019JB019150 . hal-02944805

HAL Id: hal-02944805

<https://ens.hal.science/hal-02944805>

Submitted on 21 Sep 2020

HAL is a multi-disciplinary open access archive for the deposit and dissemination of scientific research documents, whether they are published or not. The documents may come from teaching and research institutions in France or abroad, or from public or private research centers.

L'archive ouverte pluridisciplinaire **HAL**, est destinée au dépôt et à la diffusion de documents scientifiques de niveau recherche, publiés ou non, émanant des établissements d'enseignement et de recherche français ou étrangers, des laboratoires publics ou privés.

A Kalman Filter Time Series Analysis method for InSAR

M. Dalaison¹, R. Jolivet^{1,2}

¹École Normale Supérieure, PSL Université, CNRS U.M.R. 8538, Laboratoire de Géologie, Paris, France

²Institut Universitaire de France, 1 rue Descartes, 75005 Paris, France

Key Points:

- Our data assimilation method for InSAR time series analysis allows for rapid update of pre-existing models with newly acquired data.
- Errors affecting the process are accounted for, so that each estimate is associated with its relevant uncertainty.
- We provide guidelines for the parametrization of our method.

Corresponding author: Manon Dalaison, dalaison@geologie.ens.fr

Abstract

Earth orbiting satellites, such as Sentinel 1A-B, build up an ever-growing set of synthetic aperture radar images of the ground. This conceptually allows for real-time monitoring of ground displacements using Interferometric Synthetic Aperture Radar (InSAR), notably in tectonically active regions such as fault zones or over volcanoes. We propose a Kalman filter (KF) for InSAR time series analysis, an efficient method to rapidly update pre-existing time series of displacement with data as they are made available, with limited computational cost. Our KF solves together for the evolution of phase change with time and for a parametrized model of ground deformation. Synthetic tests of our KF reveal exact agreement with the equivalent weighted least-squares solution and a convergence of descriptive model parameter after the assimilation of about one year of data. We include, the impact of sudden deformation events such as earthquakes or slow slip events on the time series of displacement. First tests of the KF on ENVISAT data over Mt Etna (Sicily) and Sentinel 1 data around the Chaman fault (Afghanistan, Pakistan) show precise (± 0.05 mm) retrieval of phase change when data are sufficient. Otherwise, the optimized parametrized model is used to forecast phase change. Good agreement is found with classic time series analysis solution and GPS-derived time-series. Accurate estimates are conditioned to the proper parametrization of errors so that models and observations can be combined with their respective uncertainties. This new tool is freely available to process ongoing InSAR time series.

1 Introduction

Since the 1990s, Interferometric Synthetic Aperture Radar (InSAR) has been used and optimized to measure ground deformation from satellite [e.g. Griffiths, 1995, Burgmann et al., 2000, Simons & Rosen, 2015]. While first studies focused on temporally discrete, large amplitude events, such as earthquakes [e.g. Massonnet et al., 1993], recent geophysical applications rely on deriving the temporal evolution of deformation to capture the full spectrum of temporal behaviors, from short episodic deformation events [e.g. Lindsey et al., 2015, Rousset et al., 2016] to long-term, decadal trends [e.g. Grandin et al., 2012, Chaussard, Bürgmann, et al., 2014, Jolivet et al., 2015]. Examples include continuous monitoring of aquifers [e.g. Schmidt & Bürgmann, 2003, López-Quiroz et al., 2009, Chaussard, Wdowinski, et al., 2014], volcanoes [e.g. Pritchard & Simons, 2004, Biggs et al., 2014] slow moving landslides [e.g. Hilley et al., 2004, Scheingross et al., 2013, Tong

44 & Schmidt, 2016] or aseismic slip along active faults [e.g. Jolivet et al., 2013, Khoshmanesh
45 & Shirzaei, 2018].

46 Capturing the time evolution of ground displacement using InSAR is not direct and re-
47 quires adequate processing of sets of interferograms [e.g. Simons & Rosen, 2015]. An in-
48 terferogram is the conjugate product of two Synthetic Aperture Radar (SAR) images.
49 The corresponding interferometric phase directly records ground deformation between
50 two passes of the satellite. Reconstructing the temporal evolution of the phase, hence
51 ground deformation, through time should be straightforward. However, this procedure,
52 called time series analysis, remains a challenge as interferograms are often affected by
53 spatial and temporal decorrelation [e.g. Zebker & Villasenor, 1992, Berardino et al., 2002,
54 Simons & Rosen, 2015]. Furthermore, the reconstructed phase is the combination of var-
55 ious sources of noise such as atmospheric and ionospheric delays as well as ground dis-
56 placements. Part of the time series analysis procedure intends to separate these differ-
57 ent contributions [e.g. Burgmann et al., 2000, Emdarson et al., 2003, Agram & Simons,
58 2015].

59 Two main approaches have been developed to perform time series analysis. First, Per-
60 manent or Persistent Scatterers techniques focus on a subset of reliable pixels with sta-
61 ble backscattering properties over time to perform spatial and temporal unwrapping [e.g.
62 Ferretti et al., 2000, Hooper et al., 2007]. Second, Small Baseline Subset (SBAS) tech-
63 niques rely on the redundancy of the network of interferograms to enhance spatial cov-
64 erage and resolution [e.g. Berardino et al., 2002, Hetland et al., 2012]. In this paper, we
65 focus on SBAS techniques.

66 Temporal increments of phase change are linked to interferograms by a set of linear equa-
67 tions. As we aim to reconstruct the evolution of phase with time from interferograms,
68 we need to solve an inverse problem, which is usually done using classic least-squares [Schmidt
69 & Bürgmann, 2003, Usai, 2003, Agram et al., 2013] or singular value decomposition [Be-
70 rardino et al., 2002, López-Quiroz et al., 2009, Jolivet et al., 2012]. Nowadays, the res-
71 olution, frequency and availability of SAR images grow dramatically thanks to recent
72 launches of numerous SAR missions including the Sentinel 1A-1B (European Space Agency)
73 or the ALOS 2 (Japan Aerospace Exploration Agency) missions [Elliott et al., 2016]. Fu-
74 ture missions, such as Sentinel 1C-1D and NISAR (NASA, ISRO), will also lead to a growth
75 in the amount of available data, ensuring long temporal coverage of deformation. Ex-

76 isting SBAS techniques will inevitably become overwhelmed by the rapid accumulation
77 of images. These methods require increasing computing power and memory, as the size
78 of the inverse problem to solve grows with the quantity of observations. More importantly,
79 acquisitions at a given time do not inform on the state of deformation at another given
80 time if these epochs are not connected by interferograms. Processing the entire set of
81 interferograms each time a new acquisition is performed is not only computationally ex-
82 pensive, but also not useful.

83 We, propose a method to sequentially update pre-existing multi-annual time series of In-
84 SAR data considering only the latest observations. We describe how to use data assim-
85 ilation for the reconstruction of ground displacements using InSAR, including minimal
86 computing time and little data storage. We derive the formulation of a Kalman filter for
87 time series analysis, an approach analogous to least-squares in its assumptions and fi-
88 nal solution [Kalman, 1960, Cohn, 1997]. As data assimilation methods require accurate
89 estimation of errors at all steps, our method allows to investigate various sources of er-
90 rors.

91 Kalman filtering is already widely used to build Global Navigation Satellite System (GNSS)
92 time series [e.g. Hofmann-Wellenhof et al., 2012], as very frequent acquisition of small
93 amount of data makes such filtering very relevant. Other application in geodesy include
94 modeling of volcanic reservoir properties [e.g. Shirzaei & Walter, 2010, Bato et al., 2018]
95 or of fault slip at depth [e.g. Segall & Matthews, 1997, Bekaert et al., 2016]. Most of these
96 techniques are driven by time series of deformation in order to reconstruct the tempo-
97 ral evolution of a model describing the source of surface deformation. The aforementioned
98 methods require the use of a time series analysis method in order to reconstruct surface
99 displacements beforehand. Furthermore, although uncertainties are fundamental in any
100 assimilation scheme, uncertainties are unfortunately not always correctly estimated [Agram
101 & Simons, 2015, Bekaert et al., 2016]. Here we provide a method to continuously and
102 efficiently build InSAR time series from a stack of SAR interferograms and propagate
103 associated uncertainties.

104 In the following, we detail time series analysis for InSAR and formulate explicitly the
105 corresponding Kalman filter approach. We highlight the efficiency of our approach on
106 two different regions subjected to volcanic and tectonic deformation. We first test our
107 method on a time series of SAR acquisitions by the Envisat satellite between 2003 and

108 2010 over the Etna volcano, in Sicily, around which several GPS stations enable us to
 109 derive local time series of ground deformation. We validate our approach against this
 110 independent set of data. We also use GPS data to assess the robustness of the uncer-
 111 tainties derived by our Kalman filter implementation. We then derive a time series of
 112 ground deformation using Sentinel 1 data between 2014 and 2018 over western Pakistan
 113 and southern Afghanistan. This region is poorly instrumented and no deformation time
 114 series are available for comparison with our approach. However, vegetation cover is scarce,
 115 hence interferometric coherence is good, and the Sentinel constellation has acquired a
 116 large amount of SAR images, allowing us to highlight the efficiency of our time series
 117 analysis method.

118 **2 A Kalman filter-based approach for times series analysis**

119 **2.1 Data description and formulation of the problem**

120 The phase of an interferogram is a differential measurement of the spatial and tempo-
 121 ral change in the two way travel time of the Radar wave between the satellite and the
 122 ground. It is a direct measurement of the change in the apparent distance between the
 123 satellite and the ground, hence a function of ground deformation between two dates. Our
 124 goal is to reconstruct the evolution of the interferometric phase over time with respect
 125 to the first acquisition and to extract ground deformation from this time series. We work
 126 on each pixel independently from its neighbors [Berardino et al., 2002, Cavalié et al., 2007].
 127 For a given pixel, the unwrapped phase of the interferogram between two dates at times
 128 t_i and t_j is

$$\Phi_{ij} = \phi_j - \phi_i + \epsilon_{ij}, \quad (1)$$

129 where ϕ_j is the unwrapped phase at a time t_j relative to the phase ϕ_0 at time t_0 , and
 130 ϵ_{ij} is the error associated with the potentially inaccurate unwrapping of the interfero-
 131 metric phase, with spatial filtering and with multi-looking (i.e. non-coherent phase av-
 132 eraging often used to enhance coherence) [Goldstein et al., 1988, De Zan et al., 2015, Agram
 133 & Simons, 2015]. As interferograms connect multiple SAR acquisitions in time, we call
 134 a set of interferograms a network and ϵ_{ij} is often referred to as network misclosure [Doin
 135 et al., 2011]. Herein, the standard deviation of ϵ_{ij} will be noted σ_ϵ , assuming it is com-
 136 mon to all interferograms for simplicity.

137 Moreover, for a single pixel, the network of interferograms is often incomplete as unwrap-
 138 ping of the phase is not always possible due to spatial and temporal variations of phase
 139 coherence. If the fringe rate is too high between neighboring pixels, it is not possible to
 140 derive the relative motion of these pixels from one to another, hence phase cannot be
 141 unwrapped [Goldstein et al., 1988]. Without connectivity, it is impossible to reconstruct
 142 a common phase history between temporally disconnected sets of interferograms. Var-
 143 ious methods propose to derive a temporally parametrized model of the phase evolution,
 144 either assuming constant velocities between sub-networks [Berardino et al., 2002] or more
 145 complex ad hoc models [e.g. López-Quiroz et al., 2009, Jolivet et al., 2012, Hetland et
 146 al., 2012, Jolivet & Simons, 2018].

147 Following the approach of López-Quiroz et al. [2009], we consider a parametrized func-
 148 tion of time to describe the evolution of the interferometric phase. This function is the
 149 linear combination of a set of user-defined functions f_n of time modulated by coefficients
 150 a_n , such as the interferometric phase ϕ_i at a time t_i writes

$$\phi_i = \sum_{n=1}^N a_n f_n(t_i) + \gamma_i, \quad (2)$$

151 where γ_i is the error corresponding to mismodeling of the interferometric phase at time
 152 t_i , due to limitations of the functional model and decorrelation noise [Agram & Simons,
 153 2015]. Uncorrected atmospheric effects, such as turbulent and ionospheric delays, are the
 154 main contributions to γ_i [e.g. Doin et al., 2011, Jolivet et al., 2014]. In the following, we
 155 assume that γ_i is normally distributed with a zero mean and a standard deviation σ_γ ,
 156 assumed constant with time for simplicity. Functions f_n can be taken for instance as poly-
 157 nomial terms, Heaviside functions or periodic functions describing the time history of
 158 the interferometric phase.

159 Our goal is to solve both Equations 1 and 2 sequentially, whenever a new acquisition al-
 160 lows to compute new interferograms. We formulate an assimilation framework solving
 161 for the interferometric phase ϕ_i at each acquisition time t_i and for the terms of the parametrized
 162 function a_k and for the corresponding variances and covariances.

Symbol	Meaning	Structure	Shape
\mathbf{m}_k	state vector	$[a_0, a_1, \dots, a_{L-1}, \phi_0, \dots, \phi_k]$	$(L + k + 1)$
\mathbf{d}_k	measurement vector	$[\Phi_{fk}, \Phi_{gk}, \dots, \Phi_{hk}]$	N
\mathbf{P}_k	state covariance	–	$(L + k + 1) \times (L + k + 1)$
\mathbf{Q}_k	process noise covariance	diagonal matrix* with last element equal to $(\sigma_\gamma)^2$	$(L + k + 1) \times (L + k + 1)$
\mathbf{R}_k	observation noise covariance	diagonal matrix with $(\sigma_\epsilon)^2$ on the diagonal	$N \times N$
\mathbf{A}_k	state-transition matrix	identity matrix with additional row using a_n to forecast ϕ_k	$(L + k + 1) \times (L + k)$
\mathbf{H}_k	observation model	pairs up the phases to build the Φ_{ik} . Contains 0, 1 and -1	$N \times (L + k + 1)$

Table 1. Vectors and matrices used in the k^{th} Kalman filter iteration assimilating N interferograms (Φ_{ik}) constructed with the acquisition at time t_k . At this given step, the filter (re)estimates the $N + 1$ phases $\phi_{i,k}$ and the L parameters a_n of the linear descriptive model. (*) In our applications, diagonal elements of \mathbf{Q}_k are zero except the last one, however, it may be useful to add non-zero systematic error in the first L elements corresponding to a_n . See Appendix 7.1 for a detailed example of our KF matrices.

2.2 Setup of the Kalman filter

A Kalman filter (KF) is an iterative procedure that allows to recover the least squares solution of an inverse problem by successively adding data. For a recent and detailed introduction to Kalman filtering, readers can refer to Evensen [2009] or Carrassi et al. [2018]. Data assimilation procedures propagate and update with newly acquired data the probability density function (PDF) of a given model. In a KF, the PDF of the model is a Gaussian distribution described by a state vector, \mathbf{m} , containing mean values for model parameters and the associated covariance matrix \mathbf{P} . Each time new data is acquired, a KF proceeds in two successive steps.

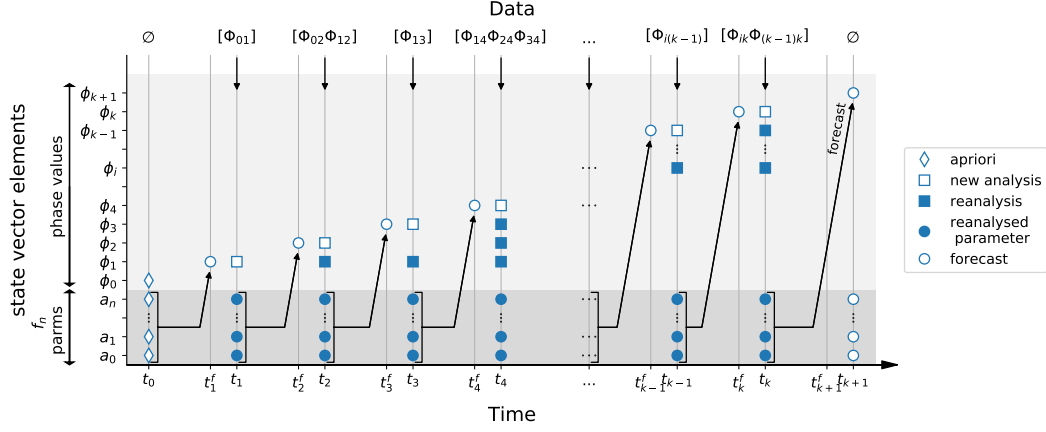


Figure 1. Scheme of the temporal evolution of the state vector as a function of assimilation time and available data. Markers highlight elements which are added or modified at a specific time-step. Additional values may be kept and stored for later reanalysis. The last step corresponds to the case when data are not available: the previous state vector is copied and the last phase is forecast using the functional description described by the parameters a_n previously estimated.

172 First, at a given time t_k , we forecast the state vector \mathbf{m}_k and its covariance matrix \mathbf{P}_k
 173 using the state vector, \mathbf{m}_{k-1} , at step $k-1$. Second, we update this forecast with the
 174 information from data acquired at time t_k in a step called analysis.

175 In practice, at a time t_k , the state vector \mathbf{m}_k includes the reconstructed phase values and
 176 the coefficients of the parametrized function of time, a_n (Figure 1). We initialize the frame-
 177 work with an *a priori* state vector, \mathbf{m}_0 and associated covariances, \mathbf{P}_0 . This *a priori* re-
 178 flects our state of knowledge on the different parameters before we input any data. Each
 179 time a new SAR image is acquired, we compute the interferograms connecting this last
 180 acquisition with previous ones, typically the four previous ones. Then, we use the func-
 181 tional form governed by the terms a_n in the current state vector to forecast the phase
 182 at the time of the new acquisition. Afterwards, we analyze the forecast with the infor-
 183 mation of the incoming data to obtain the updated state vector.

Following the marginalization rule, the forecast state vector \mathbf{m}_k^f and its covariance \mathbf{P}_k^f are given by

$$\mathbf{m}_k^f = \mathbf{A}_k \mathbf{m}_{k-1} \quad \text{and} \quad \mathbf{P}_k^f = \mathbf{A}_k \mathbf{P}_{k-1} \mathbf{A}_k^T + \mathbf{Q}_k \quad \forall k \in [1; M] \quad (3)$$

184 where \mathbf{A}_k is the state-transition matrix and \mathbf{Q}_k the process noise covariance (see Table
 185 1 for variable description). As illustrated in Figure 1, \mathbf{A}_k applied to \mathbf{m}_{k-1} computes the
 186 forecast for \mathbf{m}_k based on the latest parametric description of the time series given by a_n
 187 at time t_{k-1} (Equation 2). \mathbf{A}_k is a matrix representation of the forecast equations. In
 188 practice, phase terms of previous acquisitions and functional parameters are kept con-
 189 stant while ϕ_k^f is computed using Equation 2. Because \mathbf{A}_k is of rectangular shape, m_k^f
 190 is simply m_{k-1} augmented with the forecast phase value of the most recent acquisition.
 191 The corresponding covariance, \mathbf{P}_k^f , depends on parameter uncertainties and systematic
 192 noise included in \mathbf{Q}_k . Systematic noise in \mathbf{Q}_k represents our level of confidence in an im-
 193 perfect forecast.

We then update the state and its covariance using the available data \mathbf{d}_k at time t_k ap-
 plying Bayes' rule, so that

$$\mathbf{m}_k = \mathbf{m}_k^f + \mathbf{P}_k^f \mathbf{H}_k^T \left(\mathbf{R}_k + \mathbf{H}_k \mathbf{P}_k^f \mathbf{H}_k^T \right)^{-1} \left(\mathbf{d}_k - \mathbf{H}_k \mathbf{m}_k^f \right) \quad (4)$$

where \mathbf{R}_k is the observation noise covariance, and \mathbf{H}_k the observation model. \mathbf{H}_k is ef-
 fectively the operator predicting interferograms from the state vector \mathbf{m}_k . \mathbf{R}_k describes
 our confidence in the observation model, \mathbf{H}_k , for the data \mathbf{d}_k (hence, \mathbf{R}_k describes the
 statistics of phase misclosure, here assumed normally distributed). The analyzed vari-
 ance covariance matrix, \mathbf{P}_k , is

$$\mathbf{P}_k = \mathbf{P}_k^f - \mathbf{P}_k^f \mathbf{H}_k^T \left(\mathbf{R}_k + \mathbf{H}_k \mathbf{P}_k^f \mathbf{H}_k^T \right)^{-1} \mathbf{H}_k \mathbf{P}_k^f. \quad (5)$$

194 The term $\mathbf{P}_k^f \mathbf{H}_k^T \left(\mathbf{R}_k + \mathbf{H}_k \mathbf{P}_k^f \mathbf{H}_k^T \right)^{-1}$ is often referred to as the Kalman gain as it quan-
 195 tifies how much the predicted state “has to gain” from the difference between observed
 196 and predicted data, $\mathbf{d}_k - \mathbf{H}_k \mathbf{m}_k^f$, called residual or innovation. It also modulates the
 197 information transitioning from the covariance in the model space $\mathbf{H}_k \mathbf{P}_k^f$ to the covari-
 198 ance of the analysis. For a practical example of our KF, see the the explicit formulation
 199 in Appendix 7.1. Note that Equation 4 is the generalized least squares solution of a lin-
 200 ear inverse problem [e.g. Tarantola, 2005].

201 Because of observations equations, there is a need to keep previous estimates of phases
 202 in \mathbf{m}_k , whenever they are connected by interferograms used in the analysis step, in or-
 203 der to update phases ϕ_i ($i < k$) for all Φ_{ik} in \mathbf{d}_k (Eqn. 1 and Fig. 1). For instance, if
 204 the data contains interferograms Φ_{ak} , Φ_{bk} and Φ_{ck} we will forecast and analyze ϕ_k and

205 re-analyze ϕ_a , ϕ_b and ϕ_c using past and current observations (Figure 1). This is essen-
 206 tial to keep improving phase estimates taking advantage of the redundancy of informa-
 207 tion from all interferograms and, thus, limit the propagation of errors over time. For-
 208 mally, the re-analysis of past estimates with future data implies that the Kalman filter
 209 formulated above is effectively a Kalman smoother [Cohn et al., 1994, Cosme et al., 2012].

210 **2.3 Configuring parameters**

211 The algorithm requires user-based choices for the parametrization of the functional form
 212 and for the various covariances on a case-by-case basis. First, we have to chose a parametriza-
 213 tion for the functional form used to derive the forecast. This choice is based on our knowl-
 214 edge of deformation and simplicity of the model should be favored over precision to pre-
 215 vent overfitting.

216 Second, we need to estimate the typical standard deviation of mismodeling σ_γ for all time
 217 steps and of interferometric network misclosure σ_ϵ for all interferograms. σ_ϵ comes in the
 218 construction of \mathbf{R} because it quantifies the error between our data (interferograms) and
 219 what we are looking for (the relative phase values). It effectively acts as a regulariza-
 220 tion term when computing the Kalman gain (Table 1 and Equations 4,5). As underlined
 221 by Doin et al. [2011], covariance terms in \mathbf{R} are null because ϵ_{ij} is specific to each in-
 222 terferogram Φ_{ij} , independently of the common acquisitions $\phi_{i,j}$. Regarding σ_γ , it depends
 223 on both the simplicity of the chosen functional form and on the amplitude of unexpected
 224 atmospheric perturbations of the interferometric delay. It is directly fed into the process
 225 noise variance-covariance matrix, \mathbf{Q} , since it controls the flexibility given to the process
 226 for phase values to be different from those predicted by the chosen functional form. Typ-
 227 ically, σ_ϵ should be small with respect to σ_γ because we have greater trust in the inter-
 228 ferogram construction (Equation 1) than in the functional description of the deforma-
 229 tion (Equation 2).

230 Third, we must quantify the *a priori* mean and standard deviation of functional model
 231 coefficients a_n within the initial state vector \mathbf{m}_0 and covariance \mathbf{P}_0 . These values directly
 232 control the amplitude of the possible values for model coefficients in the analyzed state
 233 vector, and, thus, directly affect the quality of the filter’s forecast. One needs to chose
 234 large enough variances with a realistic *a priori* state vector, so that the natural spread
 235 of the variable is within one standard deviation of its mean.

236 Fourth, we can optionally add some systematic error to the parameters of the functional
 237 representation, a_n in the L first elements of the diagonal of \mathbf{Q} in order to slow down their
 238 convergence with assimilation steps. Such noise addition introduces some plasticity in
 239 the description of deformation (see Appendix 7.1). We discuss real case examples be-
 240 low to illustrate the influence of the different parameters and define a quantitative guide-
 241 line for parametrization in Section 4.1.

242 **3 Applications of the Kalman filter**

243 **3.1 Synthetic tests**

244 *3.1.1 Reference case setup*

245 In order to assess how well the Kalman filter (KF) retrieves known parameters, we gen-
 246 erate a synthetic set of InSAR data combining synthetic signal of tectonic deformation
 247 and atmospheric noise. We assess the influence of the choice of parameters and of the
 248 design of covariance matrices to validate the approach.

249 We build a two dimensional, time varying, field of phase change typical of what is ex-
 250 pected in a region crossed by a major tectonic fault. We design a synthetic acquisition
 251 planning considering a 3 years observation period with acquisitions every 12 days; sim-
 252 ilarly to what is expected for recent satellite constellations such as Sentinel 1. For each
 253 of these synthetic acquisitions, we compute synthetic unwrapped interferograms with the
 254 three preceding acquisitions using Equation 1.

255 We simulate the contributions of tectonic plate motion and shear due to interseismic load-
 256 ing along a fault (i.e slow, persistent deformation of a few cm/yr), between blocks mov-
 257 ing at 4 cm/yr with respect to each other. We add to the time series the surface displac-
 258 ements due to a typical earthquake (i.e. a discrete, large amplitude deformation event of
 259 several cm). The modeled earthquake occurs on day 500 of the time series and induces
 260 a maximum of 15 cm of displacement. In addition, we consider the case of a slow tran-
 261 sient slip event occurring on the same fault (i.e. episodic, medium amplitude deforma-
 262 tion spanning multiple acquisitions in time). This slow slip event has a temporal foot-
 263 print governed by an integrated spline function of 100-day-width centered on day 210
 264 of the time series, with a maximum cumulative displacement of 10 cm. Epicenters of both
 265 events are shown on Figure 2. All synthetic displacements are generated considering dis-
 266 locations embedded in an elastic homogeneous semi-infinite halfspace [Okada, 1992]. Fur-

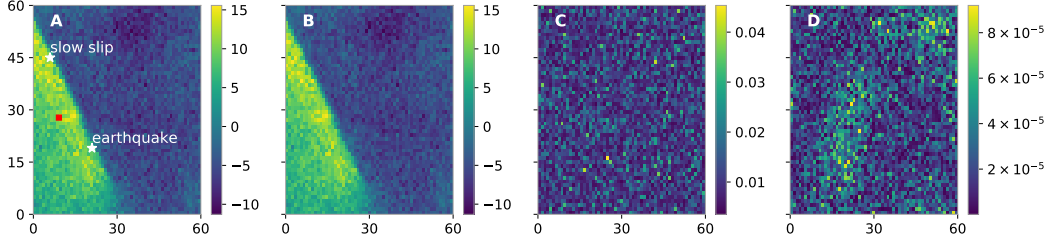


Figure 2. Performance of the Kalman filter (KF) for a two-dimensional synthetic deformation field. The phase evolution with its noise content is retrieved from noisy interferograms (i.e. non-zero network misclosure). *A* : True cumulative phase at the last time-step of the time series including deformation and correlated and uncorrelated noise. *B* : Reconstructed cumulative phase from the KF. *C* : Root Mean Square error (RMS) of the the retrieved phase (*B*) with respect to the true phase value (*A*). *D* : RMS of the phase retrieved with the KF (*B*) with respect to the least-squares solution. All scales are in centimeters to ensure the example represents a realistic case study. The location of the pixel of interest for Figure 3 is marked by a red square.

267 furthermore, we include a constant deformation rate related with interseismic loading on
 268 the main fault and seasonal oscillations (i.e. yearly sinusoidal deformation with a phase
 269 shift) of the ground everywhere. In the following tests, we aim to recover all terms of de-
 270 formation described above as well as the resulting phase evolution with our KF.

Consequently, the chosen parametrized model of the phase, ϕ_k , at a time t_k , is

$$\phi_k = a_0 + a_1 t_k + a_2 \sin\left(t_k \frac{2\pi}{T_{year}}\right) + a_3 \cos\left(t_k \frac{2\pi}{T_{year}}\right) + a_4 S_{sse}(t_k) + a_5 H_{eq}(t_k) + \gamma_k, \quad (6)$$

271 where $a_n, \forall n \in [1, 5]$, are the parameters to be solved for, T_{year} is a one year period,
 272 S_{sse} is an integrated spline function centered on day 210 with a width of 100, H_{eq} is a
 273 Heaviside function on day 500 and γ_k is the mismodeling term at time t_k with standard
 274 deviation σ_γ .

275 We first test the performance of the filter on synthetic data without any noise (imply-
 276 ing $\gamma_k = 0, \forall k$) and then on data including noise. To do so, we design a composite noise
 277 model to mimic real observations. This implies that we have, first, a spatially correlated
 278 noise reflecting atmospheric effects on each phase ‘acquisition’ and, secondly, a misclo-
 279 sure error lower by at least an order of magnitude, assuming that we have no contribu-
 280 tion from unwrapping errors [Schmidt & Bürgmann, 2003, Lohman & Simons, 2005, Cav-

281 alié et al., 2007, López-Quiroz et al., 2009, Agram & Simons, 2015]. We add spatial and
 282 temporal deviations to all parameters a_n following a random distribution with a stan-
 283 dard deviation equal to 10% of their values, and random noise on interferogram construc-
 284 tion equivalent to $\sigma_\epsilon = 0.1$ mm. Moreover, the atmospheric contribution to phase decor-
 285 relation is constructed through the convolution of a white noise, with standard devia-
 286 tion of 10 mm, and a decreasing exponential function of inter-pixel distances [Jolivet &
 287 Simons, 2018]. The specified values reflect errors observed in processed Sentinel 1 data
 288 (see Section 3.3). The resulting cumulative phase change after 3 years is shown in Fig-
 289 ure 2. The temporal evolution of phase change for one pixel is visible in Figure 3.

290 *3.1.2 Performance of the Kalman filter with optimal configuration*

291 We apply our KF with the assumption that the functional form given in Equation 6 is
 292 known. Results for simpler functional forms applied to the same synthetic data are in
 293 Figure S2 and S3. *A priori* model parameters in the initial state vector, \mathbf{m}_0 , are set to
 294 zero with standard deviations comparable to the expected spread of parameters: 10 mm
 295 for a_0 , 0.05 mm/day for a_1 , 5 mm for the *sine* and *cosine* amplitudes and 70 mm for
 296 the displacement of slip events. The first phase value for all pixels is set to zero with zero
 297 uncertainty. This means that \mathbf{m}_0 is a null vector and \mathbf{P}_0 is a diagonal matrix contain-
 298 ing the squared standard deviations listed above. When realistic noise is considered, we
 299 chose optimal parameters corresponding to the noise implemented in the synthetic data,
 300 that is $\sigma_\gamma = 10$ mm and $\sigma_\epsilon = 0.1$ mm. For comparison, we solve the full problem for
 301 all acquisitions using an equivalent least squares inversion with identical model and data
 302 covariances [Tarantola, 2005].

303 For a model without any noise (except $\sigma_\epsilon = 10^{-5}$ mm to avoid singularity of the gain),
 304 phase values are retrieved within σ_ϵ and model parameters converge after the assimi-
 305 lation of ~ 6 months of data (Figure 3A). The time required for convergence of the model
 306 parameters is justified by the fact that there is an ambiguity between the contribution
 307 of the linear and periodic terms to the deformation before reaching half the oscillation
 308 period. Regarding the earthquake, the corresponding amplitudes is found within 10^{-5}
 309 mm just after it occurred. Similarly, the amplitude of the slow slip event is retrieved once
 310 the total cumulative displacement caused by the slow slip event has been fully assimi-
 311 lated.

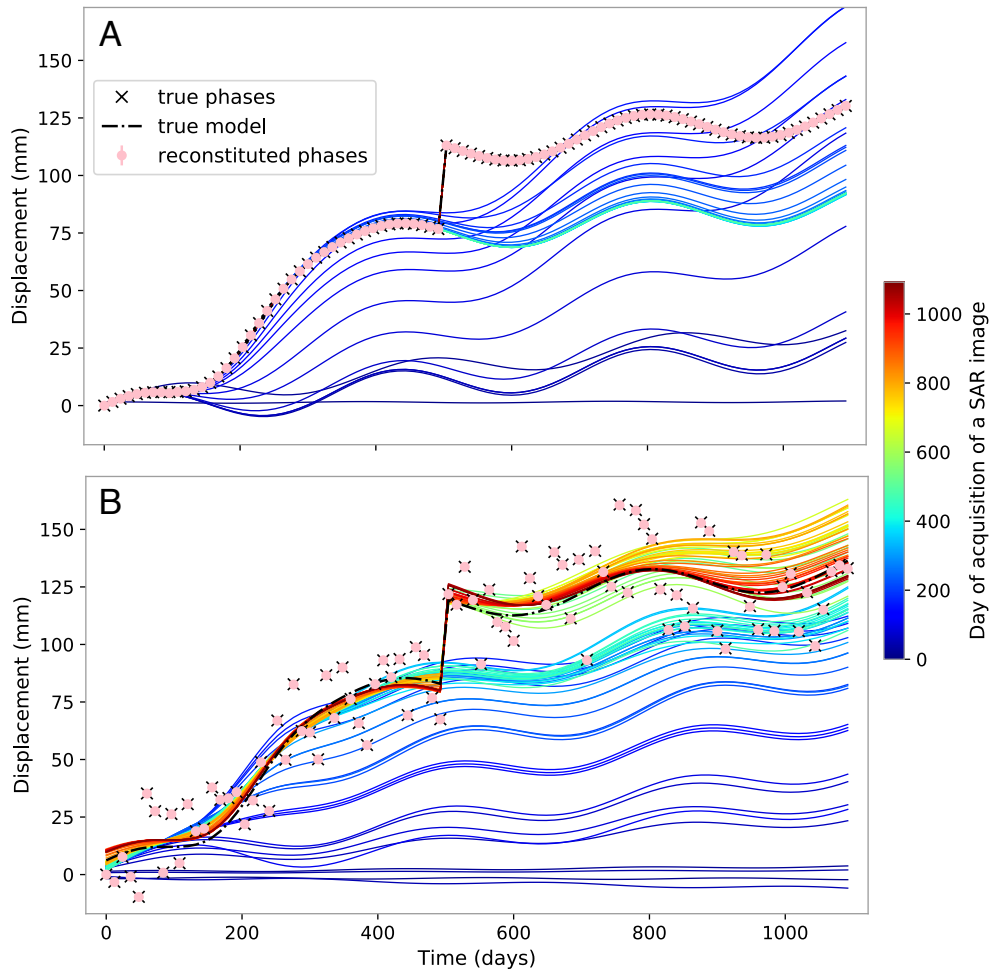


Figure 3. Time series for one pixel with temporal evolution of the model on a synthetic set of InSAR data for one pixel. *A* : case without noise in the synthetic data. *B* : same synthetic deformation but with a realistic noise model on top. Pink markers represent reconstituted phases from the Kalman filter, while black crosses are ‘true’ phases. When the phase is well retrieved, markers overlay each other and errorbars are too small to appear. Colored lines are models derived at each assimilation of a new acquisition, which date is indicated by the colorbar. Dashed black line is the true deformation. In *A*, true and reconstituted phases lie on each other and mask the underlying curves, which include the true model and computed models after day 500 (time of the modeled earthquake).

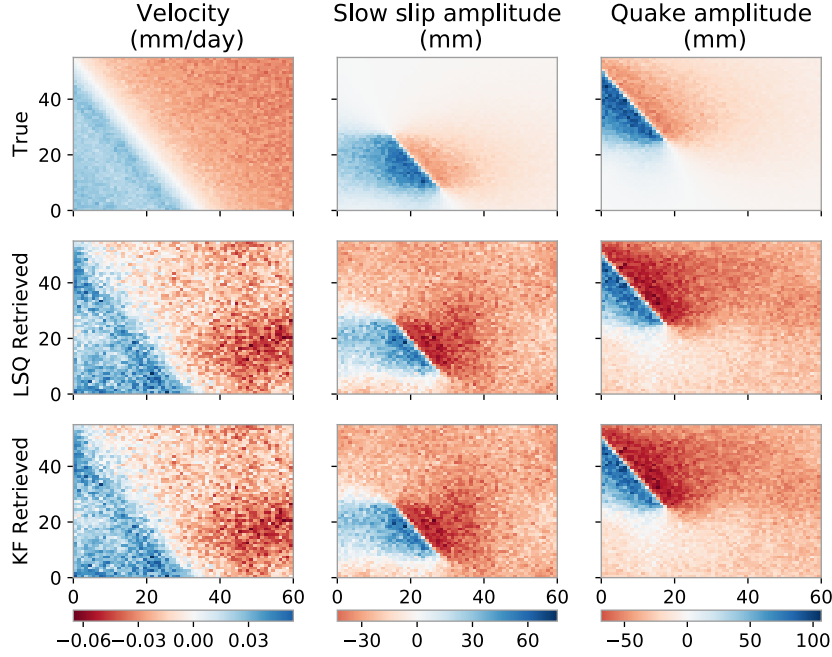


Figure 4. Maps of three of the model parameters : velocity, slow slip amplitude and quake amplitude. For comparison the true values (top), the values retrieved through least squares inversion (LSQ) (middle) and the values retrieved through Kalman filter (KF) (bottom) are displayed.

312 The final outcome of the KF is comparable with basic least squares performance (Fig-
 313 ure 2 and 4). Figure 2 shows that the KF cumulative displacement root mean square er-
 314 ror (RMS) with respect to the true displacement is on the order of σ_ϵ (0.1 mm), while
 315 it is of $\sim 10^{-5}$ cm with respect to least squares estimation. Regarding model param-
 316 eters, the difference between KF solution and target value is of ~ 1 mm, whereas it is
 317 of $\sim 10^{-3}$ mm between KF and least squares solutions. The noticeably large noise in
 318 retrieved parameters over areas with target values close to zero (Figure 4) is explained
 319 by the constant high *a priori* variance applied everywhere. Thus, if the location of the
 320 events is known, it is preferable to define a spatially variable *a priori* variance for, at least,
 321 slip events.

322 We detail here the behavior of the filter as data is assimilated in time and the require-
 323 ments for convergence. Figure 3B shows the time series of a representative pixel (located
 324 on Figure 2) and Figure 5 the associated evolution of model parameters. The functional
 325 model evolves and gains information as data are successively assimilated. Graphically,
 326 the dark blue curves combine both the *a priori* null model and the little information brought

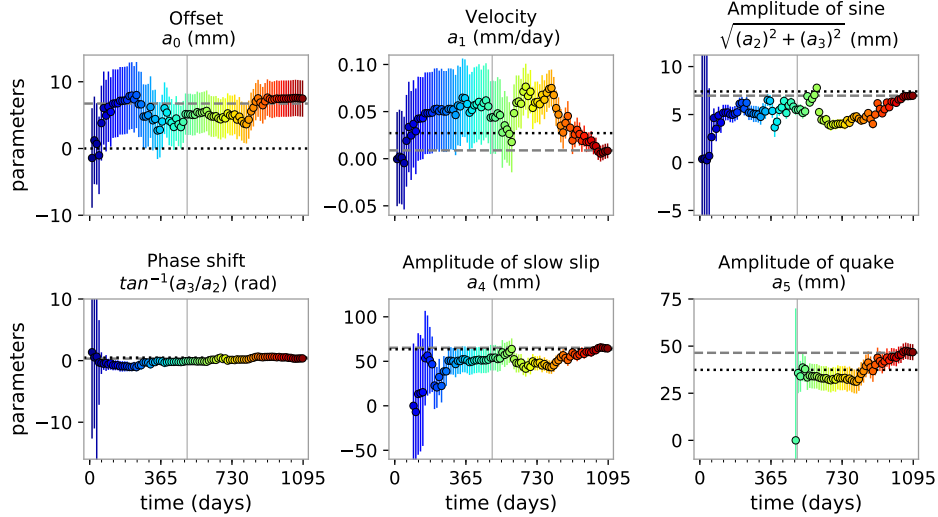


Figure 5. Temporal evolution of model functional parameters at each assimilation step for the reference pixel in our synthetic test. Colors refer to time (see colorbar in Figure 3). The amplitudes of the slow slip and the quake are added in the parameter space just before they occur. For reference, the dotted black line shows the true parameter value (i.e. target), and the dashed grey line shows the least-squares optimum. The Kalman filter solution tends toward the least-square solution, which itself depends on the interferometric network configuration and the noise in interferograms.

327 by the first few points, while the dark red curve uses all available information and closely
 328 fits the underlying model. The model progressively converges toward the least squares
 329 solution, close to the target model, at a rate that depends on how quickly parameter un-
 330 certainties collapse (Figures 3B and 5), which in turns depends on the Kalman gain (Equa-
 331 tion 5, Appendix 7.1). As shown on Figure 5, it takes about 150 days for the offset, a_0 ,
 332 to be adjusted and around one year for the yearly periodic signal, a_2 and a_3 . However,
 333 the inter-dependency of functional parameters clearly appears as variations in the tran-
 334 sient event amplitude a_4 induces a change in a_0 by 1-2 mm and the earthquake at $t =$
 335 500 days perturbs almost all parameters, including the velocity which is shifted by ~ 0.01
 336 mm/day. Correlations between parameters appear in the off-diagonal terms of the co-
 337 variance matrix (Figure S1).

338 Interestingly, we also see that, although the local earthquake amplitude a_5 of 37.4 mm
 339 was correctly retrieved after 3 assimilations ± 7 mm, the assimilation steps for $t > 750$
 340 days lead to an overestimate of a_5 and a correlated underestimate of a_1 . As interfero-

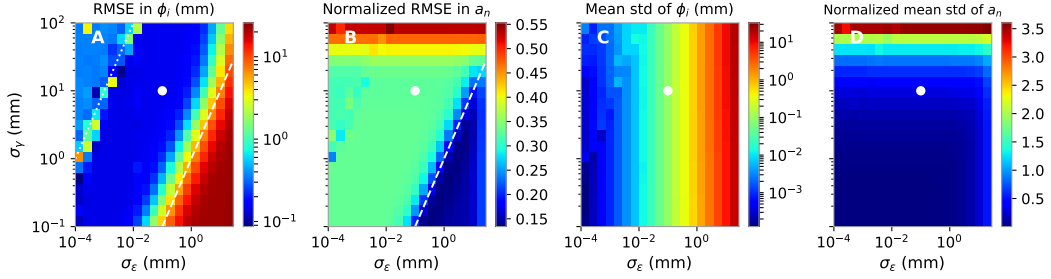


Figure 6. Errors in estimated model parameters (a_n) and phases (ϕ_i) from the Kalman Filter (KF) as a function of the standard deviation of the mismodeling noise (σ_γ) and the standard deviation of interferometric network misclosure (σ_ϵ). The true value of the noise injected in the build of the synthetic deformation is marked by the white circle. *A* and *B* reveal variations in the KF estimate accuracy by looking at the Root Mean Square Error (RMSE) in ϕ_i (*A*) and in a_n (*B*). *C* and *D* display the mean standard deviation (abr. std) of estimates. Values concerning parameters are normalized for homogeneity. The white dashed line corresponds to $\sigma_\gamma/\sigma_\epsilon = 1$ and the dotted line to $\sigma_\gamma/\sigma_\epsilon = 10^4$.

341 grams long after the event do not bring information about its amplitude, the state vec-
 342 tor \mathbf{m}_k needs to be modified. That is, to avoid fitting noise and limit trade off between
 343 parameters, functional parameters in \mathbf{m}_k can be added or removed from the procedure
 344 when relevant. Also, phases which do not appear in latter interferograms can be stored
 345 and removed from \mathbf{m}_k . This does not affect final time series and lowers the memory load
 346 of the algorithm. Practically, our KF effectively works with two storage files : one con-
 347 taining time, phases and their uncertainties (from the diagonal of \mathbf{P}_k) and another one
 348 containing \mathbf{m}_k , \mathbf{P}_k and other auxiliary information in order to run the next forecast and
 349 analysis at time t_{k+1} .

350 Nevertheless, it is a challenge to optimally parametrized the inversion with real InSAR
 351 data, especially because mismodeling and misclosure errors are generally not known [Schmidt
 352 & Bürgmann, 2003].

353 *3.1.3 Sensitivity analysis to predefined errors*

354 We study the effect of non-representative σ_γ and σ_ϵ in a sensitivity analysis, for one given
 355 pixel (shown in Figure 5 and 3). We deliberately set poorly chosen values of σ_γ and σ_ϵ
 356 in the KF with respect to the known sources of noise. Subplots of Figure 6 display how

357 4 proxies of the quality of KF estimates vary as a function of those two parameters. While
 358 Figures 6A and 6B consider the error in the absolute estimates, and thus the accuracy,
 359 Figures 6C and 6D indicate the precision (i.e. standard deviation) associated with those
 360 estimates.

The quantity displayed in 6A is the Root Mean Square error of phase estimates, and in
 6C it is the average of the posterior standard deviation of the phase estimates, σ_{ϕ_k} . The
 exact equations corresponding to fields in 6B and 6D are

$$\sqrt{\frac{1}{L} \sum_{n=1}^L \left(\frac{a_n - a_n^t}{a_n^t} \right)^2} \quad \text{and} \quad \frac{1}{L} \sum_{n=1}^L \frac{\sigma_{a_n}}{|a_n|}, \quad (7)$$

361 respectively, where the superscript t indicates target value and L is the number of pa-
 362 rameters. The first functional model parameters a_0 , a constant offset, is voluntarily ex-
 363 cluded because, first, $a_n^t = 0$ and, second, the misfit in a_0 mainly results from the re-
 364 quirement that $\phi_0 = 0$.

365 As expected from governing equations, we see that estimated standard deviations are
 366 directly impacted by choices in σ_γ and σ_ϵ . Indeed, phase uncertainties appear sensitive
 367 to σ_ϵ and model parameter uncertainties to σ_γ (Figure 6C, 6D). Another main feature
 368 is the improvement of a_n estimates at the expense of the accuracy in ϕ_k when approach-
 369 ing the domain $\sigma_\epsilon \geq \sigma_\gamma$ (Figures 6A, 6B). This is clearly not desirable, because phase
 370 estimate directly derive from interferometric data, while model parameters depend on
 371 an *ad hoc* functional description which may have to be improved as new data is assim-
 372 ilated. To the contrary, when too much confidence is given to interferograms with respect
 373 to the model (i.e. $\sigma_\epsilon \leq \sigma_\gamma \times 10^{-4}$) the effective misclosure error means that data may
 374 be hard to reconcile together and numerical instability arises. Thus, providing $\sigma_\epsilon/\sigma_\gamma$
 375 is in between 10^{-4} and 1, the quality of ϕ_k and a_n estimates appears robust to several or-
 376 ders of magnitude variations in σ_γ and σ_ϵ . We still observe an upper bound limit of \sim
 377 30 mm and \sim 15 mm for σ_γ and σ_ϵ , respectively, above which estimates are so uncer-
 378 tain that they do not adjust to the data. Time series representative of the overall effect
 379 of underestimating or overestimating σ_γ and σ_ϵ are shown in supplementary Figures (S4-
 380 S7).

381 In practice, ϵ_{ij} only results from how we construct interferograms and could be directly
 382 estimated by quantifying the effect of multilooking and filtering during the processing
 383 of each interferogram. Alternatively, it could be measured either before time series anal-

384 ysis by forming triplets of interferograms [De Zan et al., 2015, Benoit et al., 2020] or *a*
385 *posteriori* by looking at the discrepancy between real and reconstituted interferograms
386 from time series [Cavalié et al., 2007].

387 In addition to uncertainty quantification, another challenge of real InSAR data is that
388 all interferograms do not unwrap everywhere due to local loss of coherence. Consequently,
389 given pixels will potentially show missing links in the interferometric network. In the fol-
390 lowing we apply our KF to two data sets thought to be representative of the challenges
391 brought by real InSAR data.

392 **3.2 Application to the Etna Volcano on Envisat Asar images**

393 As a real case example, we first present the assimilation of interferograms over the Etna
394 volcano in Sicily. We have chosen this example as it has been used in the past for mul-
395 tiple validation studies [e.g. Doin et al., 2011, Jolivet et al., 2014] and because several
396 GNSS stations record the relatively large displacements observed over this volcano. We
397 use 63 images from the ENVISAT mission acquired between January 2003 and August
398 2010 [Doin et al., 2011]. Single Look Complex (SLC) images are focused and coregistered
399 to a single master using the Repeat Orbit Inteferometry Package [ROIPac, Rosen et al.,
400 2004]. Coregistration to a single master image is enhanced using the Digital Elevation
401 Model and all possible interferograms are derived. The 222 interferograms are filtered
402 and unwrapped using a branch cut algorithm [Goldstein et al., 1988, Goldstein & Werner,
403 1998]. We correct interferometric phase delays due to the temporal variations of the strat-
404 ified troposphere using the output of the ERA-Interim reanalysis of atmospheric data
405 as described in Jolivet et al. [2011]. All details about the processing can be found in Doin
406 et al. [2011] and in Jolivet et al. [2014].

407 We apply our Kalman filter (KF) on each pixel of the stack of images that has unwrapped
408 interferometric data. In addition to the precise retrieval of phase evolution, we aim to
409 obtain a mean rate of deformation, including potential transient events and ignoring sea-
410 sonal contributions. Hence, our parametrized model for the phase evolution includes lin-
411 ear and seasonal terms described by four parameters, a constant term, a rate of phase
412 change, a sine term and a cosine term. This model is very simplified for a volcano which
413 has undergone several eruptive events over 2003-2010. Although this may lower our pre-
414 dictive capabilities, phase estimates of uninterrupted interferometric network should not

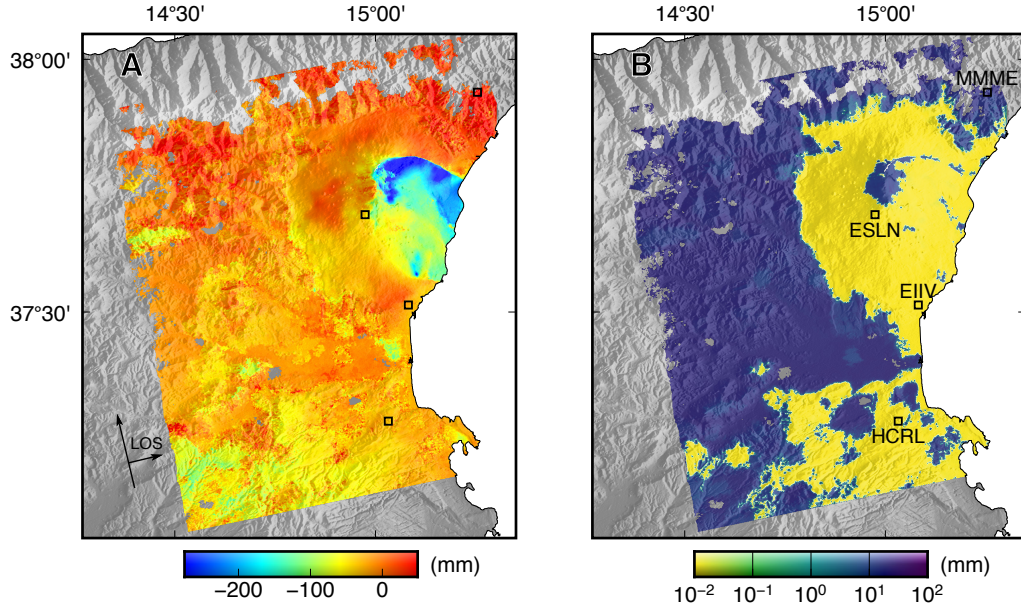


Figure 7. *A*: Map of cumulative phase change between 2003 and 2010 over Mt Etna (Sicily, Italy) as inferred from the Kalman filter time series analysis applied on ENVISAT data. *B*: Map of the associated standard deviation. Displacements and associated uncertainties are in the direction of the satellite’s line of sight (LOS). Topography, shown in the background in shades of gray, is from SRTM [Farr et al., 2007]. Holes in the data correspond to pixels excluded from the inversion because less than 20 interferograms were unwrapped at their location. Black squares show a selection of GPS station used for comparison [Blewitt et al., 2018].

415 be affected and more complex model could be applied in a second time (Section 3.1). Con-
 416 sequently, we set $\sigma_\gamma = 18$ mm and $\sigma_\epsilon = 0.01$ mm, as a high σ_γ with respect to σ_ϵ lim-
 417 its the confidence in the model-based phase forecast and keeps large uncertainties for model
 418 parameters. With the same logic, we chose *a priori* standard deviation equal to 15 mm
 419 for the constant term, 5 mm/day for velocity and 10 mm for *sine* and *cosine* terms. We
 420 set the initial state vector \mathbf{m}_0 to zeros. Note that, because the constant term reflects the
 421 noise in the reference acquisition (ϕ_0) with respect to the model, its standard deviation
 422 should be close or superior to σ_γ . The impact of different σ_γ and \mathbf{P}_0 on model param-
 423 eter estimates is displayed in Figures S11-S13.

424 We compare local time series of displacement derived from Global Navigation Satellite
 425 System (GNSS), often referred to as GPS for simplicity, at the stations EIIV, ESLN, HCRL
 426 and MMME (Figures 7 and 8; Blewitt et al. [2018]). We consider differential displace-

427 ments between two GPS stations and the equivalent closest InSAR pixel. Figure 7 shows
 428 the cumulative phase change and associated uncertainties over 8 years in the direction
 429 of the Line Of Sight (LOS) of the satellite as derived by our KF analysis at t_{61} , the 14th
 430 of July 2010. The displayed penultimate phase ϕ_{61} incorporates most of the studied de-
 431 formation with limited uncertainty as it is a reanalyse phase, unlike the last phase.

432 Standard deviations in Figure 7B are marked by a clear spatial dichotomy between the
 433 well resolved pixels displaying uncertainties $< 10^{-1}$ mm and other pixels with uncer-
 434 tainties reaching more than 10 mm. Precise estimates are available on the volcano flanks
 435 and in the urbanized region to the south, notably around stations ESLN, EIIV and HCRL
 436 and, thus, cover the area of geophysical interest. In Figure 7A, the displacement field
 437 is dominated by aseismic slip along the Pernicana fault extending from the volcano sum-
 438 mit to the eastern coast of Sicily [Palano et al., 2006]. Indeed, the fault slipped more than
 439 25 cm locally in the LOS direction over the ~ 8 years covered by the time series. Smaller
 440 coherent displacements of a few cm on the volcano flanks are also recovered. In the plains
 441 surrounding Mt Etna, cm-scale uncertainties are associated with about ± 2 cm of sharp
 442 inter-pixel variations in the displacement field.

443 Large uncertainties arise in area where more than 50% of interferograms do not unwrap
 444 due to significant spatial noise (Figure S10). When a pixel is not unwrapped, no infor-
 445 mation is available at this location and the analysis step of the filter cannot be performed.
 446 In this configuration, the forecast made from the functional model is taken as the esti-
 447 mate with its large uncertainty (i.e. $\mathbf{m}_k = \mathbf{m}_k^f$ and $\mathbf{P}_k = \mathbf{P}_k^f$). This allows to continue
 448 building the time series and to connect different subsets of interferograms which may not
 449 be linked by a common phase. However, the error associated with the forecast phase is
 450 carried forward in the subsequent solutions, if they are all relative to this one. A solu-
 451 tion to lower uncertainties is to re-reference the phases by constructing long-baseline in-
 452 terferograms.

Time series in Figure 8 evidence that the relative InSAR displacement between pixels
 close to GPS stations is consistent with what is measured independently by GPS. A mea-
 sure of the monotonicity of this relationship is given by the Spearman’s rank correlation
 coefficient for n pairs of InSAR-GPS observations, defined as

$$C_s = 1 - \frac{6}{n(n^2 - 1)} \sum_{i=1}^n d_i^2 \quad (8)$$

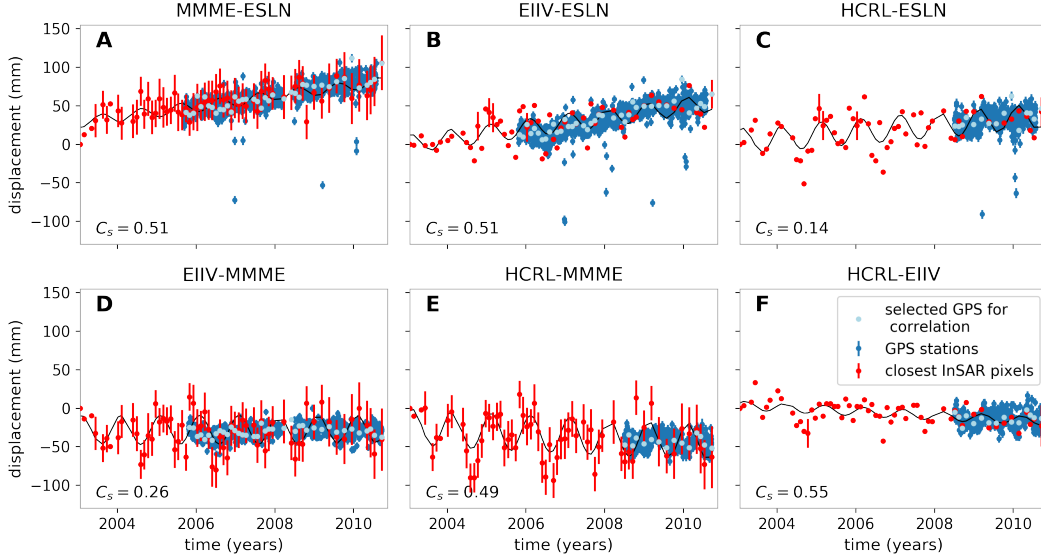


Figure 8. Overlay of GPS and InSAR time series of relative deformations. Each subplot includes the complete time series and its uncertainty for InSAR (red dots) and the available GPS time series on the same time period (blue dots). The subplot titles indicate the pair of stations located in Figure 7. The GPS data point that are temporally the closest to InSAR measurements are highlighted in light blue. They are used to compute the Spearman correlation coefficient, C_s (Equation 8). The black line is the deformation according to the functional model of the Kalman filter on InSAR.

453 where d_i is the difference between the ranks of the i^{th} coeval observations in both sets.
 454 This metric was preferred over other correlation coefficients because of its little sensi-
 455 tivity to outliers. For the 6 differential displacements considered, C_s is always positive
 456 indicating that when InSAR measures an increase, so does GPS (Figure 8). Moreover,
 457 its value close to 0.5 for 4 time series reveals a significant numerical correlation. Nonethe-
 458 less, the implications of this metric are limited because it is applied to the subset of GPS
 459 measurement coincident in time with InSAR acquisitions and both time series are af-
 460 fected by different sources of noise. Independently of the numerical correlation, the over-
 461 all good match between measured velocities validates our KF approach for InSAR time
 462 series analysis, even when the quality of data implies that errors are large (Figure 8A,
 463 8D and 8E) .

3.3 Application to the Chaman fault on Sentinel 1 images

In the following section, we illustrate the Kalman filter (KF) performance to reconstruct surface displacements around a tectonic fault imaged by a recent satellite constellation. The satellites of the Sentinel 1 mission launched in 2014 and 2015, are providing SAR images with a better temporal sampling than ever before for C-band satellites. Over the Chaman fault, we construct 364 interferograms with 95 acquisitions spanning November 2014 to May 2019. We use the ISCE package (Gurrola et al. [2010]; JPL/Caltech) to build unwrapped interferograms. We coregister SAR images with a network-based enhanced spectral diversity (NESD) approach [Fattahi et al., 2017] and remove atmospheric perturbations using ECMWF-ERA 5 global reanalysis of atmospheric data (PyAPS software; Jolivet et al. [2011, 2014]). We also multilook and filter interferograms to enhance the signal-to-noise ratio before unwrapping with the branch cut method [Goldstein et al., 1988, Goldstein & Werner, 1998]. The final size of the 2488×7024 pixels is $\sim 80 \times 130$ m. Additionally, we subtract to each interferogram a best fitting ramp (linear function of longitude and latitude) on the subregion north of the fault trace.

For comparison, we perform the time series analysis with both the well tested New Small Baseline Subset method, NSBAS [Berardino et al., 2002, Doin et al., 2011] implemented in GIAN-T [Agram et al., 2013], and the KF developed here. We chose a simple functional description of deformation with a constant deformation rate and seasonal oscillations. A disadvantage of this model is that it poorly describes deformation for specific areas affected by earthquakes or anthropogenic groundwater pumping. However, because our implementation of NSBAS does not allow for spatial variations of the parametrized model, we prefer not to account for those very local dynamics (i.e. local in comparison with our 600 km long interferograms). Our *a priori* uncertainties are 25 mm for offset, 9 mm/yr for velocity and 8 mm for cosine and sine terms. In agreement with Section 3.1.3, we chose $\sigma_\gamma = 10$ mm and $\sigma_\epsilon = 0.05$ mm. Similarly to the previous example, we focus on the reconstructed phases with time rather than on its parametrized description and display maps of the penultimate phase of the time series (Figure 9).

Final solutions from NSBAS and KF are very similar (Figure 9A and 9B). The displacement relative to the first acquisition shows a long-wavelength fault-perpendicular gradient of about 60 mm over ~ 120 km. We also observe strong negative signals with a kilometer scale footprint, such as around the city of Quetta, most likely due to aquifer-

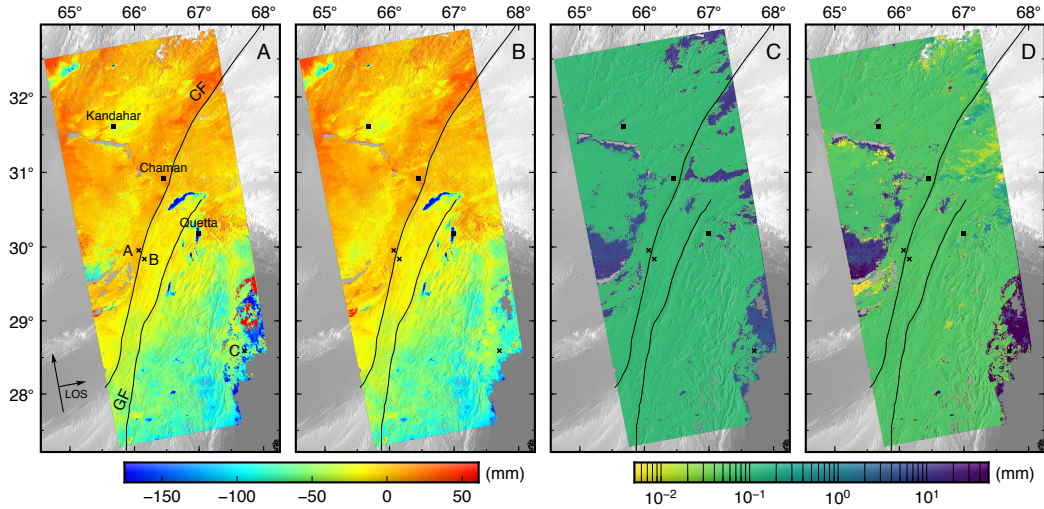


Figure 9. Maps of cumulative phase change between late 2014 and early 2019 over western Pakistan and southern Afghanistan from time series analyses applied on Track 42 data of Sentinel 1. *A*: Reference NSBAS solution, with labels of markers appearing in all subplots. *B* and *C*: Corresponding Kalman filter (KF) solution with its standard deviation. *D*: absolute difference between the NSBAS (*A*) and KF (*B*) solutions. Displacements and associated uncertainties are in the direction of the satellite’s line of sight. Two main faults of the region are the Chaman fault (CF) and the Ghazaband fault (GF) [Fattahi & Amelung, 2016]. The topography is shown in the background in shades of gray. Cities are marked by square markers. The three black crosses and letters locate the selected pixels in subplots of Figure 10.

496 related subsidence. Moreover, there is a sharp contrast of displacement across the Chaman
 497 fault which reaches up to ~ 3 cm, notably in between labeled pixels A and B or across
 498 the northernmost segment, whereas no to little contrast is seen across the Ghazaband
 499 fault. This is consistent with Fattahi & Amelung [2016] in depth study of the region.

500 The difference in phase reconstruction between both methods is smaller than 0.1 mm
 501 after the assimilation of ~ 4 years of data, except in areas where the KF identified large
 502 uncertainty in the output with respect to the ± 0.05 mm precision (equal to σ_ϵ) valid for
 503 most pixels (Figure 9C and 9D). Mismatch between NSBAS and KF methods, as well
 504 as large uncertainties in phase and model parameters concentrate around the dune desert
 505 to the West and the Indus River plain in the South-East corner. There, rapid geomor-
 506 phological changes, seasonal oscillations and human activity impose a low interferomet-
 507 ric coherence and, as a result, many interferograms could not be unwrapped there.

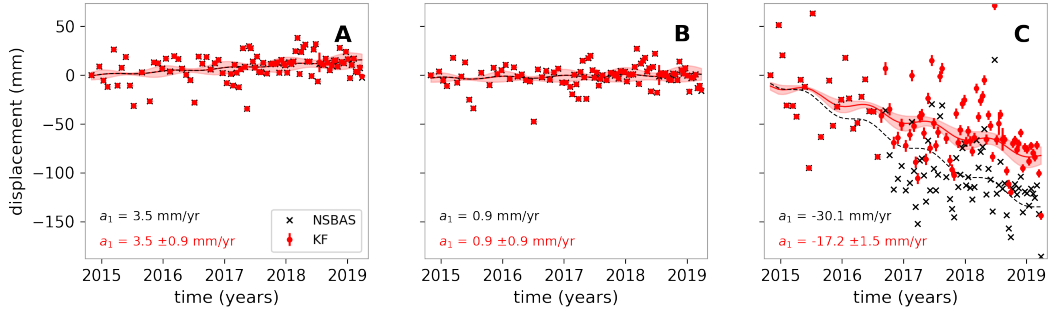


Figure 10. Time series for selected 3 pixels (indicated on Figure 9). Our Kalman filter (KF) solution with associated standard deviation (red dots) is shown alongside the solution computed with the NSBAS method [Berardino et al., 2002, Doin et al., 2011]. Most of the KF phase solutions have standard deviation too small to be visible. The corresponding functional models of deformation are also represented: dashed black curve for NSBAS and red line for KF. An idea of the spread of the models within one standard deviation of the KF solution is outlined by the red shaded area delimited by the parametrized phase evolution given $a_i \pm \sigma_{a_i}$ (Equation 2).

508 The concordance is also true at all time steps for every parameter of the state vector (dis-
 509 placements and functional model). Figure 10 presents three representative time series
 510 of deformation on single pixels. The two nearby pixels selected in Figure 10A and 10B
 511 exhibit highly correlated deformation with a spread of ~ 7 cm around the functional
 512 model. Phase estimation is precise with ± 0.05 mm and in good agreement with NSBAS
 513 estimations. For pixel A, the inferred velocity is found to be 3.5 ± 0.9 mm/yr in the KF
 514 or 3.5 in the NSBAS solution and, similarly, the seasonal amplitude and phase shift are
 515 0.9 ± 1.2 mm and 0.7 ± 0.1 rad or 0.9 mm and 0.74 rad. Those functional descriptions
 516 agree with each other and the uncertainties given by the KF are precious indicators of
 517 the model representativity and, thus, of the confidence in the resulting forecast.

518 The time series in Figure 10C exhibits large error bars of ~ 5 mm from mid-2016 aris-
 519 ing from disconnected subsets in the interferogram network. In the KF, the use of the
 520 functional model to forecast a disconnected phase and link subnetworks means that the
 521 model error propagates to subsequent phase estimations. The parametrized model of de-
 522 formation differs sensibly between NSBAS and KF methods (Figure 10), by opposition
 523 to the very good agreement found between KF and least-squares for synthetic data (Fig-
 524 ure 4). A first reason for this is the *a priori* on model parameters in the KF, which ef-
 525 fectively is a form of regularization leading to smaller velocity estimates of $a_1 = -19$

526 mm/yr instead of the physically unlikely -40 mm/yr for NSBAS. A second reason is that
 527 the NSBAS solution does not account for errors in model and data directly and instead
 528 attributes a weight to phase fitting over model adjustment, so that Equation 2 only im-
 529 pacts phase values when interferometric connections do not allow an estimate with Equa-
 530 tion 1 [Doin et al., 2011] . By definition, this weight is similar to the ratio $\sigma_\epsilon/\sigma_\gamma$, and
 531 thus was set to 10^{-3} .

532 Therefore, our Kalman filter can be applied to old, often sparse and incomplete data (EN-
 533 VISAT) as well as to most recent and memory-consuming data which are collected nowa-
 534 days (Sentinel 1).

535 4 Discussion

536 4.1 Guideline to choose parameters

537 Efficient KF requires a sensible parametrization of the problem, with the definition of
 538 appropriate errors (σ_ϵ , σ_γ), descriptive functional model ($f_n(t_k), \forall n$) and *a priori* knowl-
 539 edge on the model parameters in \mathbf{m}_0 and \mathbf{P}_0 (Section 2.3).

540 For the functional model, it is a good rule of thumb to start with a simple model, which
 541 includes a linear polynomial and an annual periodic oscillation. The innovation or resid-
 542 ual term is key to assess the relevance of this parametrized model, as it quantifies the
 543 difference between the data and the information brought by the forecast (Section 2.2).
 544 If the model is appropriate the mean innovation at each time step should have a Gaus-
 545 sian distribution around zero on each pixel (e.g. subplots B,C versus D,E in Figure S3).
 546 Thus, during the iterative process, checking the distribution of this mean innovation would
 547 help refine the parametrized model. Moreover, some source of deformation are *a priori*
 548 known and can be included. For instance, the displacements due to earthquakes affect-
 549 ing the study area can be easily included using a step function, which footprint is con-
 550 strained by the location and timing of the event in seismic catalogs. To adapt to the di-
 551 versity of applications of our KF, other implemented functions include higher degree poly-
 552 nomials, hyperbolic tangent, exponential and logarithmic decay as well as basis spline.

553 Further assumptions are required on the functional model when evaluating the *a priori*
 554 state \mathbf{m}_0 and covariance \mathbf{P}_0 . \mathbf{m}_0 and \mathbf{P}_0 define expected values of the multiplicative co-
 555 efficients a_n to each functional element f_n . Assuming a_n terms are unknown, \mathbf{m}_0 is set
 556 to zero vector with a likely spread in the diagonal of \mathbf{P}_0 . Consequently, small \mathbf{P}_0 dims

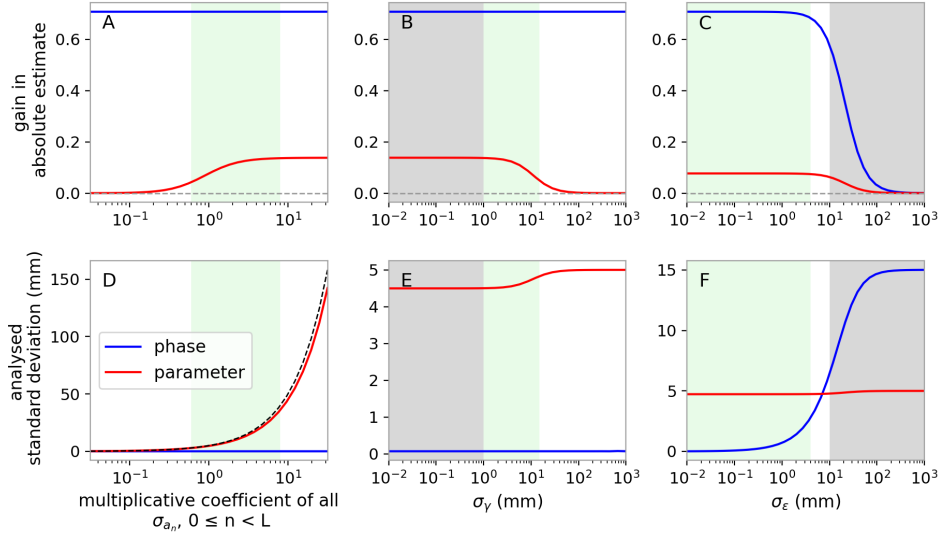


Figure 11. Variations of the gain in phase and model parameter estimates (*A-C*) and of the standard deviation of those estimates (*D-F*) as a function of the error terms used to initialize our Kalman Filter. Quantitative values are derived from Equations 3, 4 and 5 for the parametrization chose in our synthetic example. We look at one assimilation step $k=1$. The blue line is effectively ϕ_1 and the red line a_3 . Similar trends, with different amplitudes are observed for any a_n . We vary successively all σ_{a_n} (in the diagonal of \mathbf{P}_0) (*A,D*), σ_γ (*B,E*) and σ_ϵ (*C,F*). In *A,D* σ_{a_n} are multiplied by a common coefficient. The dashed grey line indicates zero gain. The black dashed line correspond to the case where σ_{a_3} evaluated at $k=1$ is the *a priori* σ_{a_3} (at $k=0$). The shaded grey area is the domain where $\sigma_\epsilon \ll \sigma_\gamma$. Green shading highlights the domains where the (i) gain on the phase is maximal, (ii) the gain on model parameter is not null (i.e. the model learns from data), (iii) the uncertainty on phase estimate is small ($\sim 10^{-2}$ mm) and (iv) the uncertainty on parameter estimate is not very large (< 40 mm). Variations in σ_γ or σ_{a_n} do not affect phase estimates. The model parameters are not adjusting to the data when the *a priori* on its standard deviation is too low or when σ_γ is too high.

557 extrema as it is effectively a regularization term for a_n , while large \mathbf{P}_0 allows paramete-
 558 rters to adjust freely to incoming data and stability might be lost (Figure 11, S8, S9 and
 559 S12). In practice, the order of magnitude of *a priori* errors is determined using our phys-
 560 ical knowledge about expected deformation. Higher values will be favored if little smooth-
 561 ing of the model is desired, however, this may lead to unrealistic forecast and very large

562 σ_{a_n} in the first few assimilation steps. The impact of the \mathbf{m}_0 and \mathbf{P}_0 will tend to van-
 563 ish as more data is assimilated.

564 Regarding the mismodeling noise γ_k and network misclosure ϵ_{ij} (Equations 1, 2), we as-
 565 sumed that they could be represented by constant standard deviations σ_γ and σ_ϵ , un-
 566 less variations in acquisition quality (e.g. seasonal noise from snow cover) or in interfer-
 567 ogram construction (e.g. varying amount of filtering) are known. Typically, we have $\sigma_\epsilon \ll$
 568 σ_γ so that phase fitting is strongly favored over parametrized model adjustment (Sec-
 569 tion 3.1.3, Figure 11). ϵ_{ij} could be measured by looking at the closure of triplets of inter-
 570 ferograms and representative σ_ϵ deduced. σ_γ should reflect the dispersion of the data
 571 around the parametrized model, which depends on the chosen model itself and the noise
 572 in the data. From previously published studies, σ_ϵ is of the order of the millimeter (as-
 573 suming no unwrapping error) and σ_γ superior to the centimeter [Schmidt & Bürgmann,
 574 2003, Cavalié et al., 2007, López-Quiroz et al., 2009, Sudhaus & Jónsson, 2009, Agram
 575 & Simons, 2015].

576 **4.2 Efficiency of the Kalman filter**

577 A main improvement of the Kalman Filter (KF) over more conventional method is the
 578 data assimilation approach. We have shown that it is capable of accurately solving the
 579 same problem than a least-squares method. However, our Kalman Filter is designed to
 580 solve other problems relevant to our ever-expanding SAR archive. First, it can actual-
 581 ize a pre-existing time-series with new interferograms in a fast and neat way. Secondly,
 582 we have built the tool in a modular and flexible manner, so that it can adapt to the evol-
 583 ving knowledge of the deformation as data is assimilated. Below, we discuss and detail
 584 those statements.

585 The iterative procedure allows fundamental discussion about the amount and shape of
 586 data necessary to obtain a meaningful description of deformation. Our tests reveal that
 587 phases are instantaneously fitted to ± 0.1 mm with later refinement as we gain informa-
 588 tion from new interferograms. Differently, model parameters require at least one year
 589 of data in order to converge, a time that depends on the variability of deformation mea-
 590 sured and how precise and accurate is our *a priori* knowledge. Velocity adjusts rather
 591 quickly, if no transient event is recorded, compared to the cosine and sine terms which
 592 require obviously more than a year. Consequently, forecast within the first year is rarely

593 accurate, which clearly reflects on the uncertainty. Once model parameters have converged
 594 toward their final value, the forecast is as good as the model is, independently of the elapsed
 595 time of assimilation. The instantaneous innovation reflects the dispersion of the data around
 596 the background model.

597 Updating pre-existing model imply a gain of time, computing power and memory. Quan-
 598 titative comparisons of computing performance of NSBAS and KF methods are not easy
 599 because their implementation are different. Indeed, our KF is implemented for simul-
 600 taneous processing of pixels in parallel by Message Passing Interface, while NSBAS uses
 601 multiple threads with shared memory in its GIANt version [Agram et al., 2013]. How-
 602 ever, it is clear that the numerical cost of updating an existing time series with the KF
 603 is much smaller than when retrieving all the phases at once with NSBAS. The time to
 604 run a KF update incorporates not only the computation time, but also the time neces-
 605 sary to read and write data and models. The latest has been optimized so that, in the
 606 example presented in Section 3.2, reconstructing phases and parameters for the 62 first
 607 dates takes 17 min, whereas updating the time series with the last acquisition takes only
 608 30 sec. As a reference, we use 2 computing nodes with 20 threads per nodes and Infini-
 609 Band communication. Concerning memory usage, previously computed interferograms
 610 do not need to be stored in order to update existing model, providing that the latest es-
 611 timates of \mathbf{m}_k and \mathbf{P}_k are available. For the example in Section 3.3, this information is
 612 stored in a HDF5 file of 6 Go, while all interferograms weigh >25 Go.

613 Another advantage of the KF is the systematic and consistent propagation of error through
 614 time series analysis. It is a requirement to correctly combine what we know from the data
 615 and from the existing model. We have seen that the absolute value of the uncertainty
 616 associated with computed phases is a consequence of the *a priori* standard deviation of
 617 misclosure (σ_ϵ) (Figure 6), which can be measured from interferograms or inferred from
 618 the way interferograms are built. Additionally, the standard deviation of mismodeling
 619 error (σ_γ) will also come into play in the case of missing data for a time step or discon-
 620 nection in the interferometric network. This error is a more subjective parameter, as it
 621 depends on the functional description chosen, and the dispersion of phases around it. Nev-
 622 ertheless, the relative uncertainty in between pixels and time steps directly results from
 623 the data structure, such as the number of interferograms available or how ‘far’ is the tem-
 624 poral reference. Those differences allow us to discriminate pixels and weight estimates
 625 for subsequent processing or modeling. This is particularly relevant for long time-series

626 (<1 year). Furthermore, covariance estimation is key to combine different data sets ,such
627 as InSAR and GPS [Bekaert et al., 2016, Sudhaus & Jónsson, 2009] or different frames
628 of InSAR acquisitions [Jolivet & Simons, 2018].

629 **4.3 Limitation and perspectives**

630 The propagation of uncertainty highlights a fundamental limit of time series analysis.
631 The time series being relative to the first date, errors tend to propagate in time. This
632 is a big issue for long time series, such as ones drawn from Sentinel 1 nowadays. Numer-
633 ous interferograms, especially those with long baselines, are necessary to limit this ef-
634 fect inherent to any classical InSAR time series analysis. Moreover, the similarity with
635 GPS time series evidenced in Section 3.2 shows the possibility of a precise re-referencing
636 of the pixel location within the time series. This has been done for vertical displacement
637 [Shirzaei & Bürgmann, 2018]. In addition, our comparison with GPS time series could
638 be improved by correcting interferograms for ionospheric effect [Simons & Rosen, 2015,
639 Liang et al., 2019].

640 The pixel by pixel approach of our KF imply that we do not account for spatial covari-
641 ance [Jolivet & Simons, 2018]. This covariance may take the form of a function of the
642 pixel-to-pixel distance, which empirically models the isotropic part of the InSAR signal
643 not due to ground deformation. Such signal mainly arises from atmospheric effects. In
644 our real case example, we limited the spatial correlation by subtracting a best-fitting
645 ramp to interferograms and by removing the stratified tropospheric delays in each in-
646 terferogram. Turbulent atmospheric delays remain, however. Nevertheless, because our
647 KF is built to deal with long time series, the temporally decorrelated contributions of
648 InSAR (e.g. turbulent delays) are reflected by the inter-acquisition dispersion for a given
649 pixel and is empirically included in the mismodeling error. This contrast with studies
650 looking at few SAR acquisitions to deal with a localized event in time [Lohman & Si-
651 mons, 2005, Sudhaus & Jónsson, 2009]. Spatial covariances are also implemented to in-
652 crease spatial continuity [Jolivet & Simons, 2018]. For our KF, we found that spatial con-
653 tinuity of phase and function parameter naturally arise from the data which only has high
654 inter-pixel noise in regions where coherence is low (e.g. Figure 10). In such region, the
655 numerous ‘holes’ in assimilated interferograms ensure low confidence in the KF estimates.
656 Spatial constrain would help gain confidence by adding more information in the prob-
657 lem but it would dramatically increase the numerical cost and would require additional

658 parametrization [Agram & Simons, 2015, Jolivet & Simons, 2018]. Additionally, the smooth-
659 ing of model parameters brought by the *a priori* ensure greater spatial continuity in low
660 coherence area with respect to NSBAS.

661 We built the Kalman filter as an accessible tool relevant to many geophysical applica-
662 tions. More specific applications will be implemented in the future, taking advantage of
663 the iterative procedure as well as systematically exploiting outputs of the KF not de-
664 tailed in this paper, such as the full temporal covariance matrix or the gain and inno-
665 vation vectors. For instance, the iterative procedure is ideal to implement automatic de-
666 tection of transient events, such as slow slip on faults. The quality of the parametrized
667 model could be systematically checked by looking at the instantaneous innovation of phase
668 values but also of model parameters. An automatic detection of non-gaussianity of the
669 innovation distribution over time could send a warning, stop the assimilation and or au-
670 tomatically update the model with predefined functions (e.g. quadratic term, Heaviside
671 function). Another major improvement of our KF would be to remove σ_γ from the pre-
672 defined parameters and include it as a parameter to be recovered during time series anal-
673 ysis.

674 **5 Conclusion**

675 We developed a tool to rapidly and efficiently update pre-existing time series of defor-
676 mation from a set of unwrapped interferograms as they are made available. The Kalman
677 filter (KF) approach is new to InSAR time series analysis and was tested on diverse sets
678 of synthetic and real interferograms in regions affected by tectonic deformations. We show
679 that the filter behaves in agreement with existing methods and GNSS measurements,
680 providing that we correctly estimate errors associated with interferograms as well as with
681 the parametrized description of deformation. We thoroughly studied and described the
682 design and impact of setup parameters. The source code is fully implemented in Python
683 3 and was built as a flexible and modular tool for the community.

684 **6 Acknowledgments**

685 This article benefited from previous works by Angélique Benoit and discussions with Dr
686 Marie Bocher, Pr Alexandre Fournier, Dr Kristel Chanard, Pr Emmanuel Cosme and
687 Theo Rebert. This work received funding from the European Research Council (ERC)
688 under the European Union's Horizon 2020 research and innovation program (Geo-4D project,

689 grant agreement 758210). Data sets used in this study are freely available online. Syn-
 690 thetic Aperture Radar images are from the PEPS platform (Sentinel 1) and from ESA
 691 Earth Online (Envisat). The digital elevation model is from NASA EarthData. ERA-
 692 5 global reanalyses of atmospheric data are distributed by the ECMWF. GPS time se-
 693 ries come from the Nevada Geodetic Laboratory website. The source code is available
 694 on Github at <https://github.com/ManonDls/KFTS-InSAR>.

695 References

- 696 Agram, P., Jolivet, R., Riel, B., Lin, Y., Simons, M., Hetland, E., . . . Lasserre, C.
 697 (2013). New radar interferometric time series analysis toolbox released. *Eos,*
 698 *Transactions American Geophysical Union, 94*(7), 69–70.
- 699 Agram, P., & Simons, M. (2015). A noise model for insar time series. *Journal of*
 700 *Geophysical Research: Solid Earth, 120*(4), 2752–2771.
- 701 Bato, M. G., Pinel, V., Yan, Y., Jouanne, F., & Vandemeulebrouck, J. (2018). Possi-
 702 ble deep connection between volcanic systems evidenced by sequential assimilation
 703 of geodetic data. *Scientific reports, 8*(1), 1–13.
- 704 Bekaert, D., Segall, P., Wright, T. J., & Hooper, A. J. (2016). A network inversion
 705 filter combining gnss and insar for tectonic slip modeling. *Journal of Geophysical*
 706 *Research: Solid Earth, 121*(3), 2069–2086.
- 707 Benoit, A., Pinel-Puysségur, B., Jolivet, R., & Lasserre, C. (2020, 03). Corphu:
 708 an algorithm based on phase closure for the correction of unwrapping errors in
 709 sar interferometry. *Geophysical Journal International, 221*(3), 1959-1970. doi:
 710 10.1093/gji/ggaa120
- 711 Berardino, P., Fornaro, G., Lanari, R., & Sansosti, E. (2002). A new algorithm
 712 for surface deformation monitoring based on small baseline differential sar in-
 713 terferograms. *IEEE Transactions on Geoscience and Remote Sensing, 40*(11),
 714 2375–2383.
- 715 Biggs, J., Ebmeier, S., Aspinall, W., Lu, Z., Pritchard, M., Sparks, R., & Mather,
 716 T. (2014). Global link between deformation and volcanic eruption quantified by
 717 satellite imagery. *Nature communications, 5*, 3471.
- 718 Blewitt, G., Hammond, W., & Kreemer, C. (2018). Harnessing the gps data explo-
 719 sion for interdisciplinary science. *Eos, 99*.
- 720 Burgmann, R., Rosen, P. A., & Fielding, E. J. (2000). Synthetic aperture radar in-

- 721 terferometry to measure earth’s surface topography and its deformation. *Annual*
722 *review of earth and planetary sciences*, 28(1), 169–209.
- 723 Carrassi, A., Bocquet, M., Bertino, L., & Evensen, G. (2018). Data assimilation in
724 the geosciences: An overview of methods, issues, and perspectives. *Wiley Interdis-*
725 *ciplinary Reviews: Climate Change*, 9(5), e535.
- 726 Cavalié, O., Doin, M.-P., Lasserre, C., & Briole, P. (2007). Ground motion mea-
727 surement in the lake mead area, nevada, by differential synthetic aperture radar
728 interferometry time series analysis: Probing the lithosphere rheological structure.
729 *Journal of Geophysical Research: Solid Earth*, 112(B3).
- 730 Chaussard, E., Bürgmann, R., Shirzaei, M., Fielding, E., & Baker, B. (2014). Pre-
731 dictability of hydraulic head changes and characterization of aquifer-system and
732 fault properties from insar-derived ground deformation. *Journal of Geophysical*
733 *Research: Solid Earth*, 119(8), 6572–6590.
- 734 Chaussard, E., Wdowinski, S., Cabral-Cano, E., & Amelung, F. (2014). Land subsi-
735 dence in central mexico detected by alos insar time-series. *Remote sensing of envi-*
736 *ronment*, 140, 94–106.
- 737 Cohn, S. E. (1997). An introduction to estimation theory (gtspecial issue\data as-
738 similation in meteorology and oceanography: Theory and practice). *Journal of the*
739 *Meteorological Society of Japan. Ser. II*, 75(1B), 257–288.
- 740 Cohn, S. E., Sivakumaran, N., & Todling, R. (1994). A fixed-lag kalman smoother
741 for retrospective data assimilation. *Monthly Weather Review*, 122(12), 2838–
742 2867.
- 743 Cosme, E., Verron, J., Brasseur, P., Blum, J., & Auroux, D. (2012). Smoothing
744 problems in a bayesian framework and their linear gaussian solutions. *Monthly*
745 *Weather Review*, 140(2), 683–695.
- 746 De Zan, F., Zonno, M., & López-Dekker, P. (2015). Phase inconsistencies and multi-
747 ple scattering in sar interferometry. *IEEE Transactions on Geoscience and Remote*
748 *Sensing*, 53(12), 6608–6616.
- 749 Doin, M.-P., Guillaso, S., Jolivet, R., Lasserre, C., Lodge, F., Ducret, G., &
750 Grandin, R. (2011). Presentation of the small baseline nsbas processing chain
751 on a case example: The etna deformation monitoring from 2003 to 2010 using
752 envisat data. In *Proceedings of the fringe symposium* (pp. 3434–3437).
- 753 Elliott, J., Walters, R., & Wright, T. (2016). The role of space-based observation

- 754 in understanding and responding to active tectonics and earthquakes. *Nature com-*
 755 *munications*, 7, 13844.
- 756 Emardson, T., Simons, M., & Webb, F. (2003). Neutral atmospheric delay in in-
 757 terferometric synthetic aperture radar applications: Statistical description and
 758 mitigation. *Journal of Geophysical Research: Solid Earth*, 108(B5).
- 759 Evensen, G. (2009). *Data assimilation: the ensemble kalman filter*. Springer Science
 760 & Business Media.
- 761 Farr, T. G., Rosen, P. A., Caro, E., Crippen, R., Duren, R., Hensley, S., ... others
 762 (2007). The shuttle radar topography mission. *Reviews of geophysics*, 45(2).
- 763 Fattahi, H., Agram, P., & Simons, M. (2017). A network-based enhanced spectral
 764 diversity approach for tops time-series analysis. *IEEE Transactions on Geoscience*
 765 *and Remote Sensing*, 55(2), 777–786.
- 766 Fattahi, H., & Amelung, A. (2016). Insar observations of strain accumulation and
 767 fault creep along the chaman fault system, pakistan and afghanistan. *Geophys.*
 768 *Res. Lett.*, 43, 8399–8406. doi: 10.1002/2016GL070121
- 769 Ferretti, A., Prati, C., & Rocca, F. (2000). Nonlinear subsidence rate estimation us-
 770 ing permanent scatterers in differential sar interferometry. *IEEE Transactions on*
 771 *geoscience and remote sensing*, 38(5), 2202–2212.
- 772 Goldstein, R. M., & Werner, C. L. (1998). Radar interferogram filtering for geophys-
 773 ical applications. *Geophysical research letters*, 25(21), 4035–4038.
- 774 Goldstein, R. M., Zebker, H. A., & Werner, C. L. (1988). Satellite radar interferome-
 775 try: Two-dimensional phase unwrapping. *Radio science*, 23(4), 713–720.
- 776 Grandin, R., Doin, M.-P., Bollinger, L., Pinel-Puysségur, B., Ducret, G., Jolivet,
 777 R., & Sapkota, S. N. (2012). Long-term growth of the himalaya inferred from
 778 interseismic insar measurement. *Geology*, 40(12), 1059–1062.
- 779 Griffiths, H. (1995). Interferometric synthetic aperture radar. *Electronics & commu-*
 780 *nication engineering journal*, 7(6), 247–256.
- 781 Gurrola, E., Rosen, P., Sacco, G., Seliga, W., Zebker, H., Simons, M., & Sandwell,
 782 D. (2010). Insar scientific computing environment. In *2010 american geophysical*
 783 *union meeting*.
- 784 Hetland, E., Musé, P., Simons, M., Lin, Y., Agram, P., & DiCaprio, C. (2012). Mul-
 785 tiscale insar time series (mints) analysis of surface deformation. *Journal of Geo-*
 786 *physical Research: Solid Earth*, 117(B2).

- 787 Hilley, G. E., Bürgmann, R., Ferretti, A., Novali, F., & Rocca, F. (2004). Dynamics
788 of slow-moving landslides from permanent scatterer analysis. *Science*, *304*(5679),
789 1952–1955.
- 790 Hofmann-Wellenhof, B., Lichtenegger, H., & Collins, J. (2012). *Global positioning*
791 *system: theory and practice*. Springer Science & Business Media.
- 792 Hooper, A., Segall, P., & Zebker, H. (2007). Persistent scatterer interferometric syn-
793 thetic aperture radar for crustal deformation analysis, with application to volcán
794 alcedo, galápagos. *Journal of Geophysical Research: Solid Earth*, *112*(B7).
- 795 Jolivet, R., Agram, P. S., Lin, N. Y., Simons, M., Doin, M.-P., Peltzer, G., & Li,
796 Z. (2014). Improving insar geodesy using global atmospheric models. *Journal of*
797 *Geophysical Research: Solid Earth*, *119*(3), 2324–2341.
- 798 Jolivet, R., Grandin, R., Lasserre, C., Doin, M.-P., & Peltzer, G. (2011). Systematic
799 insar tropospheric phase delay corrections from global meteorological reanalysis
800 data. *Geophysical Research Letters*, *38*(17).
- 801 Jolivet, R., Lasserre, C., Doin, M.-P., Guillaso, S., Peltzer, G., Dailu, R., . . . Xu,
802 X. (2012). Shallow creep on the haiyuan fault (gansu, china) revealed by sar
803 interferometry. *Journal of Geophysical Research: Solid Earth*, *117*(B6).
- 804 Jolivet, R., Lasserre, C., Doin, M.-P., Peltzer, G., Avouac, J.-P., Sun, J., & Dailu, R.
805 (2013). Spatio-temporal evolution of aseismic slip along the haiyuan fault, china:
806 Implications for fault frictional properties. *Earth and Planetary Science Letters*,
807 *377*, 23–33.
- 808 Jolivet, R., & Simons, M. (2018). A multipixel time series analysis method account-
809 ing for ground motion, atmospheric noise, and orbital errors. *Geophysical Research*
810 *Letters*, *45*(4), 1814–1824.
- 811 Jolivet, R., Simons, M., Agram, P., Duputel, Z., & Shen, Z.-K. (2015). Aseismic
812 slip and seismogenic coupling along the central san andreas fault. *Geophysical Re-*
813 *search Letters*, *42*(2), 297–306.
- 814 Kalman, R. E. (1960). A new approach to linear filtering and prediction problems.
815 *Journal of basic Engineering*, *82*(1), 35–45.
- 816 Khoshmanesh, M., & Shirzaei, M. (2018). Multiscale dynamics of aseismic slip on
817 central san andreas fault. *Geophysical Research Letters*, *45*(5), 2274–2282.
- 818 Liang, C., Agram, P., Simons, M., & Fielding, E. J. (2019). Ionospheric correction
819 of insar time series analysis of c-band sentinel-1 tops data. *IEEE Transactions on*

- 820 *Geoscience and Remote Sensing*, 57(9), 6755–6773.
- 821 Lindsey, E. O., Natsuaki, R., Xu, X., Shimada, M., Hashimoto, M., Melgar, D., &
822 Sandwell, D. T. (2015). Line-of-sight displacement from alos-2 interferometry:
823 Mw 7.8 gorkha earthquake and mw 7.3 aftershock. *Geophysical Research Letters*,
824 42(16), 6655–6661.
- 825 Lohman, R. B., & Simons, M. (2005). Some thoughts on the use of insar data to
826 constrain models of surface deformation: Noise structure and data downsampling.
827 *Geochemistry, Geophysics, Geosystems*, 6(1).
- 828 López-Quiroz, P., Doin, M.-P., Tupin, F., Briole, P., & Nicolas, J.-M. (2009). Time
829 series analysis of mexico city subsidence constrained by radar interferometry.
830 *Journal of Applied Geophysics*, 69(1), 1–15.
- 831 Massonnet, D., Rossi, M., Carmona, C., Adragna, F., Peltzer, G., Feigl, K., &
832 Rabaute, T. (1993). The displacement field of the landers earthquake mapped
833 by radar interferometry. *Nature*, 364(6433), 138.
- 834 Okada, Y. (1992). Internal deformation due to shear and tensile faults in a half-
835 space. *Bulletin of the seismological society of America*, 82(2), 1018–1040.
- 836 Palano, M., Aloisi, M., Amore, M., Bonforte, A., Calvagna, F., Cantarero, M., ...
837 others (2006). Kinematics and strain analyses of the eastern segment of the perni-
838 cana fault (mt. etna, italy) derived from geodetic techniques (1997-2005). *Annals*
839 *of Geophysics*, 49(4/5), 1105–1117.
- 840 Pritchard, M., & Simons, M. (2004). An insar-based survey of volcanic deformation
841 in the central andes. *Geochemistry, Geophysics, Geosystems*, 5(2).
- 842 Rosen, P. A., Hensley, S., Peltzer, G., & Simons, M. (2004). Updated repeat orbit
843 interferometry package released. *Eos, Transactions American Geophysical Union*,
844 85(5), 47–47.
- 845 Rousset, B., Jolivet, R., Simons, M., Lasserre, C., Riel, B., Milillo, P., ... Renard,
846 F. (2016). An aseismic slip transient on the north anatolian fault. *Geophysical*
847 *Research Letters*, 43(7), 3254–3262.
- 848 Scheingross, J. S., Minchew, B. M., Mackey, B. H., Simons, M., Lamb, M. P., &
849 Hensley, S. (2013). Fault-zone controls on the spatial distribution of slow-moving
850 landslides. *Bulletin*, 125(3-4), 473–489.
- 851 Schmidt, D. A., & Bürgmann, R. (2003). Time-dependent land uplift and subsidence
852 in the santa clara valley, california, from a large interferometric synthetic aperture

- 853 radar data set. *Journal of Geophysical Research: Solid Earth*, 108(B9).
- 854 Segall, P., & Matthews, M. (1997). Time dependent inversion of geodetic data. *Jour-*
855 *nal of Geophysical Research: Solid Earth*, 102(B10), 22391–22409.
- 856 Shirzaei, M., & Bürgmann, R. (2018). Global climate change and local land subsi-
857 dence exacerbate inundation risk to the san francisco bay area. *Science advances*,
858 4(3), eaap9234.
- 859 Shirzaei, M., & Walter, T. (2010). Time-dependent volcano source monitoring us-
860 ing insar time series: a combined genetic algorithm and kalman filter approach. *J.*
861 *Geophys. Res.*, 115, B10421.
- 862 Simons, M., & Rosen, P. (2015, 01). Interferometric synthetic aperture radar
863 geodesy. In G. Schubert (Ed.), (p. 339-385). Elsevier. doi: 10.1016/
864 B978-0-444-53802-4.00061-0
- 865 Sudhaus, H., & Jónsson, S. (2009). Improved source modelling through combined
866 use of insar and gps under consideration of correlated data errors: application to
867 the june 2000 kleifarvatn earthquake, iceland. *Geophysical Journal International*,
868 176(2), 389–404.
- 869 Tarantola, A. (2005). *Inverse problem theory and methods for model parameter esti-*
870 *mation* (Vol. 89). SIAM.
- 871 Tong, X., & Schmidt, D. (2016). Active movement of the cascade landslide complex
872 in washington from a coherence-based insar time series method. *Remote Sensing*
873 *of Environment*, 186, 405–415.
- 874 Usai, S. (2003). A least squares database approach for sar interferometric data.
875 *IEEE Transactions on Geoscience and Remote Sensing*, 41(4), 753–760.
- 876 Zebker, H. A., & Villasenor, J. (1992). Decorrelation in interferometric radar echoes.
877 *IEEE Transactions on geoscience and remote sensing*, 30(5), 950–959.

878 **7 Appendix**

879 **7.1 Explicit formulation of an example**

To explicitly present our Kalman filter (Equations 3, 4 and 5) and the design of each matrix for InSAR data (Table 1), we describe an example below. We consider the case of the Kalman filter at the 2nd assimilation of data ($k = 2$) for a linear phase model, with an offset and a velocity $\phi_i = a_0 + a_1 t_i$. The state vector, then, writes as $\mathbf{m}_1 = (a_0, a_1, \phi_0, \phi_1)$. After assimilation of data at time t_1 , we have the covariance \mathbf{P}_1 , the measurement \mathbf{A}_2 and the noise \mathbf{Q}_2 as

$$\mathbf{P}_1 = \begin{pmatrix} \sigma_{a_0}^2 & & & \\ & \sigma_{a_1}^2 & & \\ & & \sigma_{\phi_0}^2 & \\ & & & \sigma_{\phi_1}^2 \end{pmatrix}, \quad \mathbf{A}_2 = \begin{pmatrix} 1 & & & \\ & 1 & & \\ & & 1 & \\ & & & 1 \\ 1 & t_2 & 0 & 0 \end{pmatrix} \quad \text{and} \quad \mathbf{Q}_2 = \begin{pmatrix} q_0 & & & \\ & q_1 & & \\ & & 0 & \\ & & & 0 \\ & & & & \sigma_\gamma^2 \end{pmatrix}. \quad (9)$$

880 Because we want to exactly reconstruct phases with respect to a fixed null starting phase,
 881 ϕ_0 , then σ_{ϕ_0} must be set to zero. The parameters q_0 and q_1 are non-zero if there is a need
 882 to add systematic noise for functional parameters $a_{0,1}$. This would relax the weight of
 883 the previous estimate of $a_{0,1}$ on each forecast.

We consider two interferograms, $\phi_2 - \phi_0$ and $\phi_2 - \phi_1$, from 3 acquisitions at times t_0 , t_1 and t_2 . Thus the data, observation model \mathbf{H}_2 and covariance \mathbf{R}_2 are given as

$$\mathbf{d}_2 = (\Phi_{02}, \Phi_{12}), \quad \mathbf{H}_2 = \begin{pmatrix} 0 & 0 & 0 & 0 & 1 \\ 0 & 0 & 0 & -1 & 1 \end{pmatrix} \quad \text{and} \quad \mathbf{R}_2 = \begin{pmatrix} \sigma_\epsilon^2 & 0 \\ 0 & \sigma_\epsilon^2 \end{pmatrix} \quad (10)$$

Applying Equations 3,

$$\sigma_{\phi_2}^f = \sqrt{\sigma_{a_0}^2 + \sigma_{a_1}^2 t_2^2 + \sigma_\gamma^2}. \quad \text{and} \quad \phi_2^f = a_0 + a_1 t_2 \quad (11)$$

884 Note that, if data is sufficient, the phase ϕ_1 would have been reconstructed at the pre-
 885 vious step with little uncertainty, so that $\sigma_{\phi_1} \rightarrow 0$. Following this assumption and us-
 886 ing the data in d_2 , we update the forecast with Equations 4 and 5. As an example, we
 887 have

$$(\sigma_{\phi_2})_{k=2} = \sqrt{(\sigma_{\phi_2}^f)^2 - 2\kappa(\sigma_{\phi_2}^f)^4} \quad \text{and} \quad (\phi_2)_{k=2} = \phi_2^f + \rho\kappa(\sigma_{\phi_2}^f)^2 \quad (12)$$

$$(\sigma_{a_1})_{k=2} = \sqrt{\sigma_{a_1}^2 - 2\kappa\sigma_{a_1}^4 t_2^2 + q_0} \quad \text{and} \quad (a_1)_{k=2} = a_1 + \rho\kappa\sigma_{a_1}^2 t_2 \quad (13)$$

with κ the common part of the gain to all analyzed parameters and ρ the residual expressed as

$$\kappa = \frac{1}{\sigma_\epsilon^2 + 2(\sigma_{\phi_2}^f)^2} \quad \text{and} \quad \rho = \Phi_{02} + \Phi_{12} + (\phi_1)_{k=1} - 2\phi_2^f \quad (14)$$

888 The subscript ‘k=2’ outlines that the values are those evaluated at the second assimi-
 889 lation step. The velocity a_1 will be re-analyzed at each assimilation step and the phase
 890 ϕ_2 may be re-analyzed if interferogram(s) Φ_{2k} for any k are assimilated over the course
 891 of subsequent assimilation steps. If noise associated with interferogram construction is
 892 small (i.e. $\sigma_\epsilon \rightarrow 0$), then Equation 12 tells us that the phase at time t_2 is perfectly re-
 893 constructed with zero uncertainty. In a more general sens, Equations 12 and 13 evidence
 894 the dependency of any phase and model parameter estimate to error terms arising from
 895 governing Equations 3, 4 and 5 (see Figures 11).